

Study on the Number of Independent Beams from Planar Domains

by

Roderick Giosevan Tapia Barroso

In partial fulfilment of the requirements for the degree of

MASTER OF SCIENCE

In

ELECTRICAL ENGINEERING

Supervisors:

Prof. dr. ing. A. Neto,

Dr. D. Cavallo,

R. Ozzola

January 17, 2023

Terahertz Sensing Group
Department of Microelectronics
Faculty of Electrical Engineering, Mathematics and Computer Science
Delft University Of Technology

*Dedicado a mis padres,
Giovana y Jose*

Abstract

Future communication scenarios will require massive Multiple-input multiple-output (MIMO) by the use of multi-beam antenna systems. Maximizing the number of beams for a given antenna size is paramount given that the space allocated to the antenna is often limited. This work aims at evaluating the maximum number of beams by analyzing the SIR in different communication scenarios for planar antenna structures. The concept of ‘observable field’ is used to quantify the power received from the desired signal as well as the power associated with the interference. Due to the planarity of the considered antenna structures, the radiating domains introduce scan loss, an effect not previously modelled when considering earlier investigations based on spherical domains. Furthermore, methods of reducing interference in order to improve the SIR were investigated, i.e., the use of a tapered current distributions on the radiating apertures and null placement techniques.

Acknowledgements

I would like to thank my supervisors Prof. Andrea Neto, Dr. Daniele Cavallo and Riccardo Ozzola for their immense support during this project. I have learned so much from you and I'm grateful to have been under your guidance for this past year. Thank you Riccardo, for the many discussions, chats, and fun.

Thank you as well to other professors at the Terahertz Sensing group, Prof. Nuria LLombart and Prof. Angelo Freni, for the fruitful discussions and advice. To all the members of the Terahertz Sensing group, thank you for your collaboration and the atmosphere you create. It is amazing to be surrounded by such capable individuals, from whom I learn something new everyday.

To my friends at the honours programme, the International Space University, CERN, from high school in Aruba, thank you all for your support during these past few years. I'm glad to have met all of you and to call you my friends.

To my friends in Delft who have become like my family, a mere few characters on a thesis is not enough to describe how thankful I am to have you. My life here would have not been the same without you, thank you for all your patience and love, I never imagined how much I would need you. When I needed you the most, there was always someone there for me.

Y a mi familia, que es lo mas importante en mi vida. A mis padres, Giovana y Jose, gracias por sus esfuerzo, sacrificio y amor. A mi hermano Josje, quien es una maravillosa persona, a quien admiro y me motiva a ser mejor persona. A mi familia en Peru, mis tios y primos, gracias por su apoyo y siempre desearme lo mejor.

This Page Intentionally Left Blank

Contents

1	Introduction	1
1.1	Background	1
1.2	Contribution of this Thesis	2
1.3	Thesis Outline	2
2	The Observable Field	5
2.1	The Definition of the Observable Field	5
2.2	The Observable Field as a Spherical Modes Expansion	6
2.3	The Observable Field Using Physical Optics	9
2.3.1	The Amplification Factor	10
2.3.2	Far Field Radiation	12
2.4	The Observable Field from Specific Shapes	13
2.4.1	Sphere	13
2.4.2	Rectangular Domain	15
2.4.3	Planar Circular Domain	19
3	Number of Beams Analysis	25
3.1	Coupling Coefficients	25
3.1.1	Integration on the Far Field Sphere	26
3.2	Signal-to-Interference Ratio Modelling	29
3.3	Randomly Distributed Clients	32
3.4	Maximum Number of Beams	33
4	SIR Improvement Techniques	37
4.1	Tapered Distribution	37
4.2	Nulling	39
5	Conclusions and Future Work	45
5.1	Summary and Conclusions	45
5.2	Future Work	46
A	Observable Field for Generalized Incidence	47
A.1	The Generalized Amplification Factor	47
B	Radiation from a Rectangular Aperture	51
C	Radiation from a Circular Aperture	53
D	Radiation from a Tapered Distribution	57

1. Introduction

1.1 Background

Wireless data traffic has been increasing exponentially in recent years, due to the proliferation of user terminals and bandwidth-greedy services, e.g., the continual use of video streaming and data-intensive applications. This huge data volume has forced the wireless industry to move to its fifth generation (5G) of cellular network, to find new techniques to offer unprecedented speeds in wireless communications.

A key characteristic of future base stations is the possibility to transmit and receive multiple data streams through directive beams connecting the base station with different users. With the advent of 5G communications and the planning for future 6G networks, antennas will focus the radiation in smaller angular regions with the aim to improve the energy and spectral efficiency, while reducing interference levels. Base station will implement massive Multiple-input multiple-output (MIMO)[1],[2] by the use of multi-beam antenna systems [3], as usually employed in satellite-based communication [4–8]. In such systems, the efficient use of the allocated space to the antenna is of paramount importance. The volume available for the antenna is often limited because several frequency bands need to be covered, leading to many antennas competing for the same space on the base station.

One of the challenges for wireless network design is maximizing the number of users simultaneously served by the base station with the required Signal to Interference Ratio (SIR), while minimizing the volume containing the antenna. Recently, the antenna community has started addressing these challenges by investigating the theoretical limits for the maximum number of independent beams that can be supported by a platform of a given size. These studies include analyses based on the degrees of freedom [9],[10], integral equation solvers [11],[12], spherical wave expansions [13], and circuit theory [14].

The usual future communication scenario considers multiple users transmitting simultaneously to the base station, each establishing a data stream interfering with each other, as depicted in Fig. 1.1. When considering a given client's data stream as the desired signal, all other data streams are

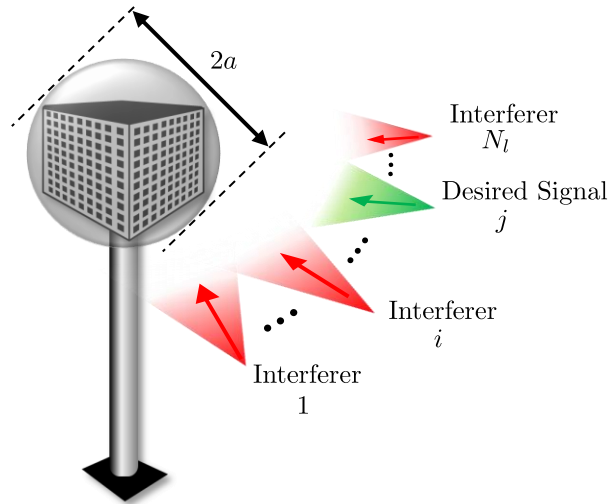


Figure 1.1: Depiction of a multi-beam LoS scenario with N_l simultaneous links, each associated with an incident beam.

considered to be interferers. Links are assumed independent of each other if the SIR is maintained above a certain threshold level. Mutual coupling between beams in a communication scenario

can limit the maximum number of independent clients a platform can host [15]. Previous works analyzing satellite-based multi-beam communications rely on the use of the aperture efficiency as the main parameter for assessing the performance since the structures considered are large in terms of wavelength. However, when considering structures whose size is comparable to the wavelength, the concept of the aperture efficiency is no longer useful since for antennas of size comparable to or smaller than the wavelength the aperture efficiency becomes larger than one. Hence, current methodologies are not valid for platforms of moderate size. To this aid, the concept of the observable field derived by using Physical Optics (PO) currents was introduced in [16], which is the part of the incident field that can be received by an antenna contained in a given volume. In [17], the observable field was exploited to calculate how much power an antenna with a given radiation pattern can receive. This was possible by the introduction of coupling coefficients that correlate the observable field with the pattern of the antenna under analysis. The structures considered in [16–18] are, however, spherical structures, which are not practical antenna structure realizations.

1.2 Contribution of this Thesis

In this thesis we extend the concept of the observable field, as introduced in [16], to arbitrarily shaped domains, focusing on the practical relevance of planar domains. In this work the clients are considered to be Line-of-Sight (LoS) in the far field region for which the beams of the clients are assumed to be plane waves.

The effective area predicted by the observable field as derived using spherical mode expansions is compared with the recently introduced PO currents approach, for which the latter provides a continuous power available to the structure in relation to the size. The derivation of the observable field using the PO currents is presented for arbitrary structures and the need for an amplification factor, which ensures the power scattered by the field radiated by the PO currents is the same as the power available to the antenna, is clarified. The theory derived for arbitrary geometries is applied to planar rectangular and circular domains.

The observable field derived using the PO currents is used to calculate the SIR in different communication scenarios, for the case of the two planar domains and in comparison to the case of the sphere. The extensive SIR analysis for the different communication scenarios requires the numerical evaluation of multiple integrals. To accelerate the calculation of these, the Gauss - Legendre quadrature scheme was implemented. Using the SIR, the total number of independent beams that can be hosted by a given antenna size is calculated.

Furthermore, this work presents two improvement techniques to improve the SIR. By using a tapered distribution instead of a uniform distribution the resulting radiation pattern, with a lower sidelobe level, can reduce the interference, and consequently improve the SIR, for structures larger than a certain size. Secondly, a null placement technique in the antenna pattern is presented to reduce the contribution of interference by a given user located at a certain angle.

1.3 Thesis Outline

This thesis consists of three main chapters. In Chapter 2, the observable field as derived by the spherical mode expansions is explained (Sec. 2.2). The observable field using the PO current is derived for arbitrary structures in Sec. 2.1 and the need for the amplification factor α with its derivation, are presented. The theory for arbitrary structures is then applied to planar domains, which are of practical relevance. In Subsec. 2.4.2 a rectangular structure is considered and in Subsec. 2.4.3 a planar circular structure is considered. Different structure sizes are analyzed and compared to the previously analyzed spherical case.

In Chapter 3, the number of beams that can be hosted by a given platform is analyzed. This

is done by the introduction of coupling coefficients in Sec. 3.1, that calculate the power available from a given incident field. The Gauss - Legendre quadrature scheme is presented in Subsec. 3.1.1. The modelling of the SIR can be found in Sec. 3.2, where the planar structures are compared to the spherical case. Furthermore, the maximum number of beams allowed for a given antenna size can be found in Sec. 3.4. The effects on the SIR of randomly distributed clients is analyzed in Sec. 3.3.

In Chapter 4, two techniques are presented to improve the SIR. The use of a tapered distribution is compared to the use of a uniform distribution in Sec. 4.1. In Sec. 4.2, the use of a null placement technique in the antenna pattern is compared to the case of using the pattern resulting from uniform currents radiating the same pattern as the one of the observable field.

Finally, in Chapter 5 conclusions are presented and the future work is discussed.

This Page Intentionally Left Blank

2. The Observable Field

This chapter presents the concept of the observable field, i.e. the part of the incident field that can be received by an ideal antenna having finite dimensions. The importance of thoroughly understanding the process of receiving antennas is linked to the optimization of the antenna gain, and its physical bounds [10, 19–21]. However, uncertainties still exist in fundamental characteristics of antennas, such as the maximum power available to antennas having finite dimensions. To this aim, in [21] the maximum gain of an antenna of arbitrary size was derived by using the spherical harmonics. By means of the mode expansion, it was possible to isolate the low-order spherical modes, i.e., the ones which propagate and that can actually interact with the antenna, and the high-order modes, that are in cut-off and cannot interact with the given size antenna. However, the discrete number of modes used to represent the fields implies a non-continuous behavior that creates uncertainty for resonant-size structures.

In [10], a *heuristic* approach is used to obtain the maximum antenna gain continuous with respect to the antenna size. However, [10] presents a model based on the interpolation of powers, making it inapplicable to the case when multiple plane waves impinge on the structure.

In the present thesis, the approach of [16] is used to model the maximum antenna gain, by means of the Physical Optics (PO) currents distributed over the domain of interest.

2.1 The Definition of the Observable Field

The observable field is the portion of the incident field that contributes to the power received by the ideal antenna allocated within a given volume. As such, the incident electric field can be represented as the superposition of the observable field \vec{E}_{obs} and the remaining field \vec{E}_{rem} as

$$\vec{E}_{\text{inc}} = \vec{E}_{\text{obs}} + \vec{E}_{\text{rem}}. \quad (2.1)$$

The power P_{obs} , associated with the observable field \vec{E}_{obs} , is the maximum power that can be received by an antenna contained in a finite-size domain. Furthermore, the observable field can be expressed as the superposition of an inward- and an outward-propagating spherical wave, expressed as follows

$$\vec{E}_{\text{obs}} = \vec{E}_{\text{obs}}^{\text{inw}} + \vec{E}_{\text{obs}}^{\text{out}}. \quad (2.2)$$

The inward and the outward component can be written as follows

$$\vec{E}_{\text{obs}}^{\text{inw/out}}(\vec{r}) = \vec{V}_{\text{obs}}^{\text{inw/out}}(\hat{k}) \frac{e^{\pm jkr}}{r} \quad (2.3)$$

where $\vec{V}_{\text{obs}}^{\text{inw/out}}(\hat{k})$ is the far field pattern of the field. Given a body located at the center of the reference system and a plane wave impinging on it, the inward component of the observable field is a spherical wave that converges towards the origin and emerges out of it with the outward-propagating component, leaving the polarization unperturbed. The outward and the inward components are related as follows

$$\vec{V}_{\text{obs, TM}}^{\text{out}}(\theta, \phi) = \vec{V}_{\text{obs, TM}}^{\text{inw}}(\pi - \theta, \phi + \pi) \quad (2.4a)$$

$$\vec{V}_{\text{obs, TE}}^{\text{out}}(\theta, \phi) = -\vec{V}_{\text{obs, TE}}^{\text{inw}}(\pi - \theta, \phi + \pi) \quad (2.4b)$$

where the subscripts “TE” and “TM” refer to the transverse electric and the transverse magnetic components of the field, respectively.

The model of the observable field is connected with the synthesis of the antenna that maximises the available power for a given incident field. Let us consider the incident electric and magnetic fields \vec{E}_{inc} , \vec{H}_{inc} impinging on an arbitrary antenna, as sketched in Fig. 2.1a, and whose inward and outward propagating observable field for the electric field are sketched in Fig. 2.1b. The ideal antenna that maximises the received power must scatter a field \vec{E}_{scat} which is equal and opposite in

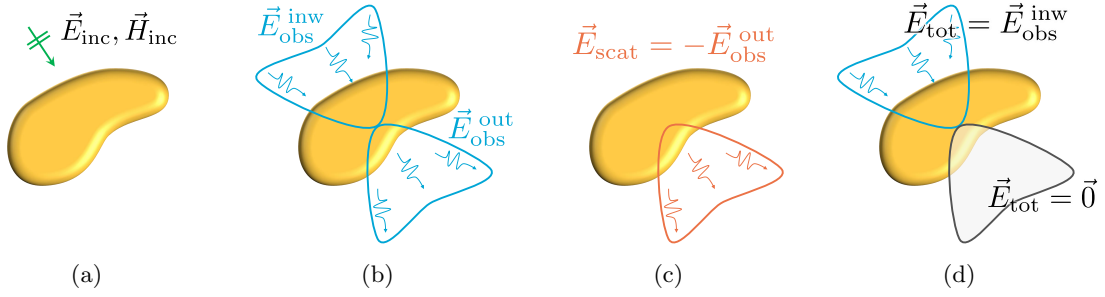


Figure 2.1: Scattering problem of the ideal antenna where (a) a plane wave impinges on an arbitrary antenna structure, (b) this plane wave has an inward and outward observable field, (c) the ideal antenna is the one scattering the outward observable field in opposite phase (d) nullifying the diverging component of the total field.

phase to the outward observable field \vec{E}_{obs}^{out} (see Fig. 2.1c), such that the total field $\vec{E}_{tot} = \vec{E}_{obs} + \vec{E}_{scat}$ has no diverging component (see Fig. 2.1d), [16, 21].

In the case of a plane wave having electric field amplitude E_0 , the maximum available power can be related to the maximum effective area A_{eff}^{max} with the following expression

$$P_L^{max} = \frac{1}{2\zeta} |E_0|^2 A_{eff}^{max} = P_{scat}^{max} \quad (2.5)$$

or equivalently to the maximum directivity D^{max}

$$A_{eff}^{max} = \frac{\lambda^2}{4\pi} D^{max}. \quad (2.6)$$

Hence, the problem of estimating the maximum effective area is equivalent to estimating the maximum directivity.

2.2 The Observable Field as a Spherical Modes Expansion

In [21] the maximum directivity of a finite size antenna was derived by means of a spherical mode expansion. This approach indirectly acknowledged the existence of the observable field \vec{E}_{obs} , as the field associated with the N_{sp} propagating spherical modes, contributing to the available power, and the remaining field \vec{E}_{rem} associated with the cut-off modes.

The incident field \vec{E}_{inc} and \vec{H}_{inc} , i.e., the field propagating in absence of the structure, is considered to be a plane wave travelling along the negative \hat{z} direction, expressed as follows

$$\vec{E}_{inc} = E_0 e^{jkz} \hat{x} \quad (2.7a)$$

$$\vec{H}_{inc} = -\frac{E_0}{\zeta} e^{jkz} \hat{y} \quad (2.7b)$$

where E_0 is the electric field amplitude, and ζ is the characteristic impedance of the medium. One can expand an incident field in terms of spherical harmonics [21, 22] obtaining the following expressions

$$\vec{E}_{inc} = E_0 \sum_{n=1}^{\infty} \sum_{m=0}^n \left(A_q^i \vec{M}_q^{(1)} + B_q^i \vec{N}_q^{(1)} \right) \quad (2.8)$$

$$\vec{H}_{inc} = \frac{jE_0}{\zeta} \sum_{n=1}^{\infty} \sum_{m=0}^n \left(B_q^i \vec{M}_q^{(1)} + A_q^i \vec{N}_q^{(1)} \right) \quad (2.9)$$

where \vec{M} and \vec{N} are the vector harmonic wave functions as defined in [21, 22], the subscripts q are the compact notation for mn (i.e., the indexes of the two sums) with the addition of “e” or “o” for even and odd modes respectively, the superscripts are associated with the radial dependence $z_n^{(i)}$ corresponding to the spherical Bessel function of the 1st kind j_n , the spherical Bessel function of the 2nd kind y_n , the spherical Hankel function of the 1st kind $h_n^{(1)}$ and the spherical Hankel function of the 2nd kind $h_n^{(2)}$ for $i = 1, 2, 3$ and 4, respectively. Outside the domain of the antenna, the scattered fields can be represented as

$$\vec{E}_{\text{scat}} = E_0 \sum_{n=1}^{\infty} \sum_{m=0}^n \left(A_q^s \vec{M}_q^{(4)} + B_q^s \vec{N}_q^{(4)} \right) \quad (2.10)$$

since the scattered field propagates outwardly, the superscript 4, which stands for the spherical Hankel function of the 2nd kind, is chosen for the radial dependence. The total power delivered to the load can be written as follows

$$P_L = \sum_{n=1}^{\infty} \sum_{m=0}^n (P_q^{\text{TE}} + P_q^{\text{TM}}) \quad (2.11)$$

i.e., as the sum of the power associated with each order of spherical TE and TM modes, due to the orthogonality between different modes and orders. The power carried by each order q can be expressed by the flux of the Poynting vector associated with each mode through the closed surface S , as follows

$$P_q^{\text{TE}} = \text{Re} \left\{ \frac{j|E_0|^2}{2\zeta} \iint_S \left(A_q^i A_q^{i*} \vec{M}_q^{(1)} \times \vec{N}_q^{(1)*} + A_q^i A_q^{s*} \vec{M}_q^{(1)} \times \vec{N}_q^{(4)*} + \right. \right. \\ \left. \left. A_q^s A_q^{i*} \vec{M}_q^{(4)} \times \vec{N}_q^{(1)*} + A_q^s A_q^{s*} \vec{M}_q^{(4)} \times \vec{N}_q^{(4)*} \right) \cdot \hat{r} dS \right\} \quad (2.12)$$

$$P_q^{\text{TM}} = \text{Re} \left\{ \frac{j|E_0|^2}{2\zeta} \iint_S \left(B_q^i B_q^{i*} \vec{N}_q^{(1)} \times \vec{M}_q^{(1)*} + B_q^i B_q^{s*} \vec{N}_q^{(1)} \times \vec{M}_q^{(4)*} + \right. \right. \\ \left. \left. B_q^s B_q^{i*} \vec{N}_q^{(4)} \times \vec{M}_q^{(1)*} + B_q^s B_q^{s*} \vec{N}_q^{(4)} \times \vec{M}_q^{(4)*} \right) \cdot \hat{r} dS \right\}. \quad (2.13)$$

Using the orthogonality relationships as described in [21], the total received power can be written as

$$P_L = -\frac{|E_0|^2}{2k^2\zeta} \sum_{n=1}^{\infty} \sum_{m=0}^n \lambda_{mn} \left(\text{Re}\{A_q^{i*} A_q^s\} + \text{Re}\{B_q^{i*} B_q^s\} + |A_q^s|^2 + |B_q^s|^2 \right) \quad (2.14)$$

where

$$\lambda_{mn} = \frac{2\pi\varepsilon_m}{2n+1} n(n+1) \frac{(n+m)!}{(n-m)!} \quad (2.15)$$

with $\varepsilon_m = 2$ when $m = 0$ and $\varepsilon_m = 1$ otherwise. By calculating the maximum of (2.14) with respect to the expansion coefficients of the scattered field A_q^s and B_q^s , the maximum occurs when

$$A_q^s = -\frac{1}{2} A_q^i \quad (2.16a)$$

$$B_q^s = -\frac{1}{2} B_q^i \quad (2.16b)$$

yielding a maximum power P_L^{\max} expressed as follows

$$P_L^{\max} = \frac{|E_0|^2}{8k^2\zeta} \sum_{n=1}^{\infty} \sum_{m=0}^n \lambda_{mn} (|A_q^i|^2 + |B_q^i|^2). \quad (2.17)$$

Under the optimum receiving conditions the total field, which is the sum of the incident and scattered field, takes on the following radial dependence

$$j_n - \frac{1}{2}h_n^{(2)} = \frac{1}{2} [h_n^{(1)} + h_n^{(2)}] - \frac{1}{2}h_n^{(2)} = \frac{1}{2}h_n^{(1)}. \quad (2.18)$$

It can be seen that the total field is a radially converging wave. Hence, in the optimum receiving scenario the scattered field cancels the outward-propagating component of the incident field.

If the incident field is the one expressed in (2.7a) (2.7b), the coefficients of the modal expansion can be calculated by resorting to [22], yielding the following result

$$A_{omn}^i = \delta_{m1} j^n \frac{2n+1}{n(n+1)}, \quad A_{emn}^i = 0 \quad (2.19a)$$

$$B_{omn}^i = 0, \quad B_{emn}^i = -\delta_{m1} j^{n+1} \frac{2n+1}{n(n+1)} \quad (2.19b)$$

where δ_{m1} is the Kronecker delta. By substituting (2.19) into (2.17), the maximum power becomes as follows

$$P_L^{\max} = \frac{\pi|E_0|^2}{2k^2\zeta} \sum_{n=1}^{\infty} (2n+1). \quad (2.20)$$

Due to the infinite number of modes used in (2.20), the maximum power results being unbounded. This is due to the fact that an infinite number of modes is needed to create a scattered field able to cancel the incident field. However, as is known [23], the spherical modes of order $N > ka$ decay rapidly for a domain of size a . Hence, the sum in (2.20) is truncated at the mode $N = [ka]$, and thus becomes as follows

$$P_L^{\max} = \frac{\pi|E_0|^2}{2k^2\zeta} (N^2 + 2N). \quad (2.21)$$

The expression (2.21), corresponds to the maximum effective area

$$A_{\text{eff}}^{\max} = \frac{\lambda^2}{4\pi} (N^2 + 2N). \quad (2.22)$$

In the case of large aperture antennas one can see that $N \approx ka \gg 1$, which gives a maximum effective area

$$A_{\text{eff}}^{\max} \approx \frac{\lambda^2}{4\pi} (ka)^2 = \pi a^2 \quad (2.23)$$

which is the physical area of the aperture. Hence, for electrically large antennas, the effective area approaches the physical area as expected. In the case of electrically small antennas, only one mode is retained, therefore, the maximum effective area becomes

$$A_{\text{eff}}^{\max} = \frac{3\lambda^2}{4\pi} \quad (2.24)$$

which is the effective area of the Huygens source.

A limitation of this approach is that due to the fact that the fields are represented in terms of spherical modes, the maximum power that can be received has a quantized behaviour, which especially in the case of antennas with size in the order of fractions of wavelength is an inadequate approximation [10, 24], as can be seen from Fig.2.2. Furthermore, the retention of the first N_{sp} modes implies radiating currents which are not bounded to the antenna domain [16], yielding a more difficult synthesis of the antenna patterns from the given size.

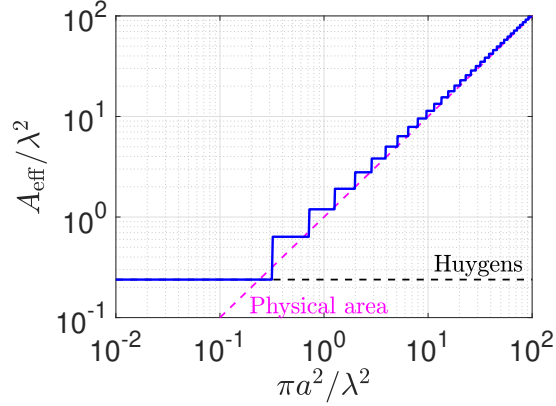


Figure 2.2: Maximum effective area of a spherical domain of radius a calculated using the spherical modes compared with the physical area of the domain, and the effective area of a Huygens source.

2.3 The Observable Field Using Physical Optics

An alternative approach to the spherical mode expansion of Sec. 2.2, is to describe the observable field as the one radiated by the equivalent currents calculated over the domain of interest [16]. Hence, the maximum directivity achievable from the given domain is associated with the antenna whose radiating currents are equal to the ones radiating the inward observable field. This method used to calculate those currents is by resorting to the Physical Optics (PO) currents [16–18]. This is a technique that resorts to the equivalence theorem, replacing a scattering problem by an equivalent problem using equivalent currents. In the case of a plane wave, an infinite surface would be necessary to sustain currents that would radiate a plane wave. However, the PO method used here employs a truncation in space, limited to the illuminated portion of the structure, rendering this a finite problem. The equivalent currents resulting from the PO method are as follows

$$\vec{J}_{\text{PO}}^{\text{out}} = \begin{cases} -\hat{n} \times \vec{H}_{\text{inc}}, & \text{if } \hat{n} \cdot \hat{k}_{\text{inc}} < 0 \\ 0 & \text{otherwise} \end{cases} \quad (2.25)$$

$$\vec{M}_{\text{PO}}^{\text{out}} = \begin{cases} \hat{n} \times \vec{E}_{\text{inc}}, & \text{if } \hat{n} \cdot \hat{k}_{\text{inc}} < 0 \\ 0 & \text{otherwise} \end{cases} \quad (2.26)$$

where \hat{n} is the outwardly-pointing normal vector, as shown in Fig. 2.3. To calculate the currents that radiate a field with a similar pattern as the inward observable field, the following transformation can be used

$$\vec{J}_{\text{PO}}^{\text{inw}}(\vec{r}) = -\left(\vec{J}_{\text{PO}}^{\text{out}}(\vec{r})\right)^* \quad (2.27a)$$

$$\vec{M}_{\text{PO}}^{\text{inw}}(\vec{r}) = \left(\vec{M}_{\text{PO}}^{\text{out}}(\vec{r})\right)^* \quad (2.27b)$$

where $*$ represents the complex conjugate.

However, the PO approach does not guarantee that the power radiated by $\vec{J}_{\text{PO}}^{\text{out}}$ and $\vec{M}_{\text{PO}}^{\text{out}}$ is equal to the one that can be received by the ideal antenna. Hence, in order to calculate the currents

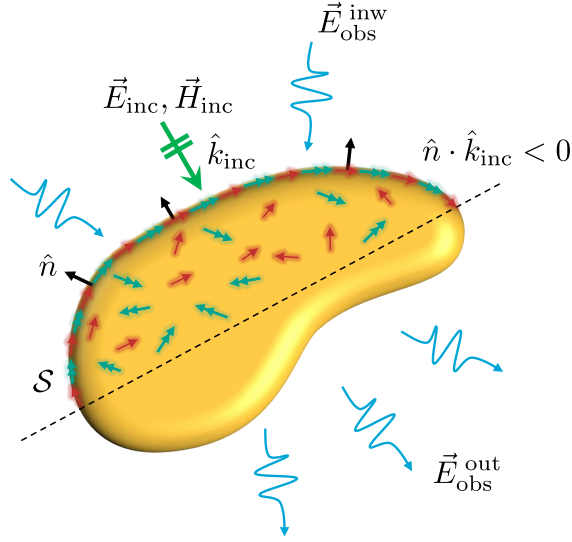


Figure 2.3: Sketch of an incident field impinging from direction \hat{k}_{inc} , into a domain enveloped by a surface S . The components of the incident field interacting with the structure is represented by an inward and outward propagating observable field, calculated using PO currents on S .

that give rise to the observable field, the scaling factor α is introduced as follows

$$\vec{J}_{obs}^{inw/out}(\vec{r}) = \alpha \vec{J}_{PO}^{inw/out}(\vec{r}) \quad (2.28a)$$

$$\vec{M}_{obs}^{inw/out}(\vec{r}) = \alpha \vec{M}_{PO}^{inw/out}(\vec{r}). \quad (2.28b)$$

This accounts for the fact that in the case of small antennas in terms of the wavelength their effective area is much larger than their physical area. The procedure to calculate the amplification factor α is the topic of Subsec. 2.3.1.

The presented methodology can be applied to any geometry, e.g., a TM plane wave impinging from $\theta_i = 45^\circ$ and $\phi_i = 45^\circ$ on a cube of edge size λ , as shown in Fig. 2.4. The results of the time domain PO currents for such a scenario are depicted in Fig. 2.5. It can be seen that, as expected, the PO currents are non-zero for the illuminated part of the structure while they are zero in the non-illuminated part.

Even though the derivation of PO currents assumes a plane wave incidence, the methodology is easily extendable for a generalized incidence by performing a plane wave expansion, as described in Appendix A.

2.3.1 The Amplification Factor

The procedure to calculate the amplification factor, called α here, has been amply described in [16] and [18]. In the plane wave incidence case, we can define the amplification factor by using the directivity. The directivity achieved by the PO currents is

$$D_{PO} = 4\pi \frac{\frac{1}{2\zeta} \left| \vec{V}_{PO}^{out}(\hat{k}_{inc}, \hat{k}) \right|_{\max}^2}{P_{PO}}, \quad (2.29)$$

where $\left| \vec{V}_{PO}^{out}(\hat{k}_{inc}, \hat{k}) \right|_{\max}^2$ is the maximum of the observable field pattern associated with the structure under analysis when a plane wave is impinging from \hat{k}_{inc} , and P_{PO} is the power radiated by the PO

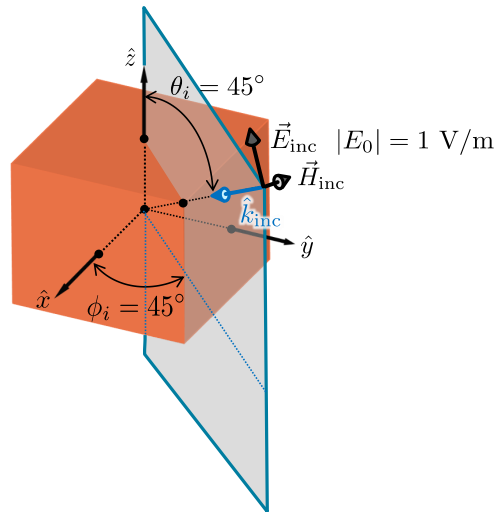


Figure 2.4: Cube structure under plane wave incidence.

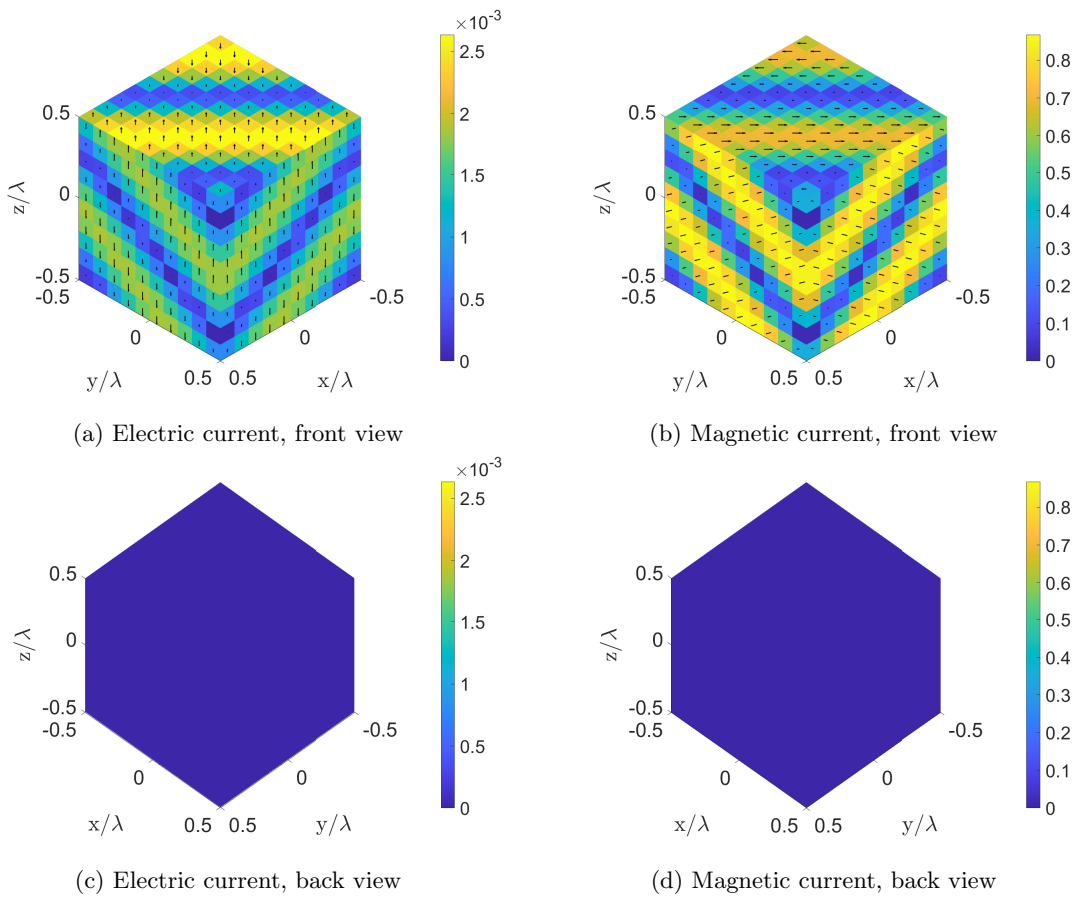


Figure 2.5: Electric (a) and magnetic (b) PO currents on the illuminated faces and electric (c) and magnetic (d) PO currents on the shadow region of a cube of edge λ .

currents. Equivalently, the associated effective area is

$$A_{\text{eff,PO}} = \frac{\lambda^2}{4\pi} D_{\text{PO}} = \lambda^2 \frac{\frac{1}{2\zeta} \left| \vec{V}_{\text{PO}}^{\text{out}}(\hat{k}_{\text{inc}}, \hat{k}) \right|_{\text{max}}^2}{P_{\text{PO}}}. \quad (2.30)$$

Therefore, the power radiated by the PO currents can be written as follows

$$P_{\text{PO}} = \lambda^2 \frac{\frac{1}{2\zeta} \left| \vec{V}_{\text{PO}}^{\text{out}}(\hat{k}_{\text{inc}}, \hat{k}) \right|_{\text{max}}^2}{A_{\text{eff,PO}}}. \quad (2.31)$$

If the amplification factor is taken into account, the ideal scattered power becomes $P_{\text{scat}}^{\text{ideal}} = \alpha^2 P_{\text{PO}}$. Recalling that the maximum available power received by an antenna illuminated by a plane wave is

$$P_{\text{rec}}^{\text{max}} = \frac{1}{2\zeta} |E_0|^2 A_{\text{eff}}^{\text{max}} \quad (2.32)$$

and by using (2.31), the amplification factor α results as follows

$$\alpha = \frac{|E_0| A_{\text{eff,PO}}}{\lambda \left| \vec{V}_{\text{PO}}^{\text{out}}(\hat{k}_{\text{inc}}, \hat{k}) \right|_{\text{max}}}. \quad (2.33)$$

The amplification factor for a generalized incidence can be found in Appendix A.1.

2.3.2 Far Field Radiation

The fields radiated by electric and magnetic currents located in an unbounded, isotropic, homogeneous medium can be calculated as follows

$$\vec{E}(\vec{r}) = -j\omega\mu \iiint_V \underline{\underline{G}}^e(\vec{r}, \vec{r}') \cdot \vec{J}(\vec{r}') d\vec{r}' - \iiint_V \underline{\underline{G}}^m(\vec{r}, \vec{r}') \cdot \vec{M}(\vec{r}') d\vec{r}' \quad (2.34)$$

$$\vec{H}(\vec{r}) = -j\omega\epsilon \iiint_V \underline{\underline{G}}^e(\vec{r}, \vec{r}') \cdot \vec{M}(\vec{r}') d\vec{r}' - \iiint_V \underline{\underline{G}}^m(\vec{r}, \vec{r}') \cdot \vec{J}(\vec{r}') d\vec{r}' \quad (2.35)$$

where

$$\underline{\underline{G}}^e(\vec{r}, \vec{r}') = \left[\underline{\underline{I}} + \frac{\vec{\nabla} \vec{\nabla}}{k^2} \right] g(\vec{r} - \vec{r}') \quad (2.36)$$

$$\underline{\underline{G}}^m(\vec{r}, \vec{r}') = \vec{\nabla} g(\vec{r} - \vec{r}') \times \underline{\underline{I}} \quad (2.37)$$

are the electric and magnetic dyadic Green's functions, respectively, for an unbounded, isotropic, homogeneous medium and

$$g(\vec{r} - \vec{r}') = \frac{e^{-jk|\vec{r} - \vec{r}'|}}{4\pi|\vec{r} - \vec{r}'|} \quad (2.38)$$

is the scalar Green's function. Since in telecommunications, the clients are usually located in the antenna far field, the radiation integrals (2.34) and (2.35) can be approximated as follows

$$\vec{E}(\vec{r}) = -j\omega\mu \frac{e^{-jkr}}{4\pi r} (\underline{\underline{I}} - \hat{r}\hat{r}) \cdot \iint_S \vec{J}(\vec{r}') e^{j\vec{k}\vec{r}'} d\vec{r}' + jk \frac{e^{-jkr}}{4\pi r} \hat{r} \times \iint_S \vec{M}(\vec{r}') e^{j\vec{k}\vec{r}'} d\vec{r}' \quad (2.39)$$

$$\vec{H}(\vec{r}) = \sqrt{\frac{\epsilon}{\mu}} \hat{r} \times \vec{E}(\vec{r}) \quad (2.40)$$

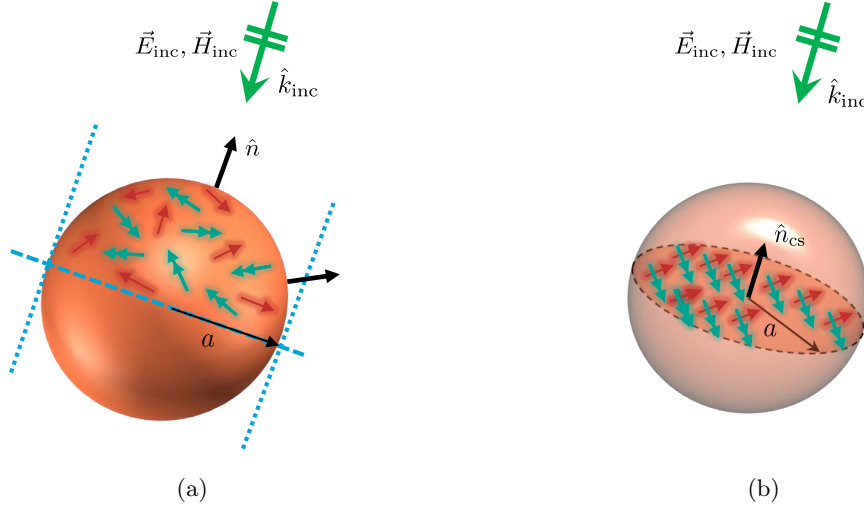


Figure 2.6: PO currents for a spherical surface, defined over (a) the illuminated hemisphere and (b) the surface currents over the cross-sectional disk radiating the same observable field.

where surface current distributions have been considered. The approximations leading to (2.39) and (2.40) allow a maximum phase error of $\pi/8$ and a maximum amplitude error of 5% if the observation point \vec{r} satisfies the following conditions

$$\begin{cases} |\vec{r} - \vec{r}'| \gg \frac{\lambda}{\pi} \\ r > 10D \\ r > \frac{2D^2}{\lambda} \end{cases} \quad (2.41)$$

where D is the diameter of the structure.

2.4 The Observable Field from Specific Shapes

2.4.1 Sphere

In order to establish a comparison with the previous work, the observable field for spherical structures is repeated in this thesis. This type of structure has been previously analyzed in [16], [18] and [17]. More specifically, the procedure to derive the pattern of the observable field for such a structure has been presented in [16]. Using the PO approach we can define the currents on a hemispherical surface, the portion of the sphere that is illuminated by the impinging plane wave. The currents defined on this domain would necessarily radiate the same field as the currents defined over the circular surface representing the sphere's cross-section [16, 18]. When the currents are defined over the sphere's cross-section the problem becomes one of solving the radiation from uniform sources with constant phase defined on a circular domain perpendicular to the direction of the impinging plane wave as illustrated in Fig. 2.6.

In order to calculate the radiation from such a structure we assume a plane wave impinging from the \vec{k}_{inc} direction with polarization \hat{p}_{inc} as follows

$$\vec{E}_{\text{inc}} = |E_0| e^{-j\vec{k}_{\text{inc}}\vec{r}'} \hat{p}_{\text{inc}}. \quad (2.42)$$

Therefore, (2.39) can be written as

$$\begin{aligned} \vec{E}_{\text{obs}}^{\text{out}}(\vec{r}) &= j\omega\mu \frac{e^{-jk r}}{4\pi r} (\underline{\underline{I}} - \hat{r}\hat{r}) \cdot \iint_S \alpha \frac{1}{\zeta} |E_0| \hat{n}_{\text{cs}} \times (\hat{k}_{\text{inc}} \times \hat{p}_{\text{inc}}) e^{j\vec{k}\vec{r}'} d\vec{r}' \\ &\quad - jk \frac{e^{-jk r}}{4\pi r} \hat{r} \times \iint_S \alpha |E_0| (\hat{n}_{\text{cs}} \times \hat{p}_{\text{inc}}) e^{j\vec{k}\vec{r}'} d\vec{r}'. \end{aligned} \quad (2.43)$$

By recognizing that $\omega\mu/\zeta = k$, and by rearranging the terms

$$\vec{E}_{\text{obs}}^{\text{out}}(\vec{r}) = jk\alpha |E_0| \frac{e^{-jk r}}{4\pi r} \iint_S e^{j\vec{k}\vec{r}'} d\vec{r}' \left[(\underline{\underline{I}} - \hat{r}\hat{r}) \cdot \hat{n}_{\text{cs}} \times (\hat{k}_{\text{inc}} \times \hat{p}_{\text{inc}}) - \hat{r} \times (\hat{n}_{\text{cs}} \times \hat{p}_{\text{inc}}) \right] \quad (2.44)$$

where S is the circular surface. Following (2.3) we can write the pattern $\vec{V}_{\text{obs}}^{\text{out}}$ of the outward observable field as

$$\vec{V}_{\text{obs}}^{\text{out}}(\hat{k}) = \frac{jk\alpha |E_0|}{4\pi} \iint_S e^{j\vec{k}\vec{r}'} d\vec{r}' \left[(\underline{\underline{I}} - \hat{r}\hat{r}) \cdot \hat{n}_{\text{cs}} \times (\hat{k}_{\text{inc}} \times \hat{p}_{\text{inc}}) - \hat{r} \times (\hat{n}_{\text{cs}} \times \hat{p}_{\text{inc}}) \right]. \quad (2.45)$$

The integral in (2.45) can be closed analytically as follows

$$\iint_S e^{j\vec{k}\vec{r}'} d\vec{r}' = 2\pi a^2 \frac{J_1(ka \sin \gamma)}{ka \sin \gamma} \quad (2.46)$$

with a being the radius of the sphere and $\gamma = \cos^{-1}(\hat{k} \cdot \hat{k}_{\text{inc}})$ the angle between the direction of incidence and the direction of observation. Therefore the pattern of the outward observable field can be written as

$$\vec{V}_{\text{obs}}^{\text{out}}(a, \hat{k}_{\text{inc}}, \hat{k}) = \frac{jk\alpha |E_0|}{4\pi} 2\pi a^2 \frac{J_1(ka \sin \gamma)}{ka \sin \gamma} \left[(\underline{\underline{I}} - \hat{r}\hat{r}) \cdot \hat{n}_{\text{cs}} \times (\hat{k}_{\text{inc}} \times \hat{p}_{\text{inc}}) - \hat{r} \times (\hat{n}_{\text{cs}} \times \hat{p}_{\text{inc}}) \right]. \quad (2.47)$$

Recalling the property of the observable field as in (2.4a) and (2.4b) we can calculate the pattern of the inward component of the observable field as

$$\vec{V}_{\text{obs}}^{\text{inw}}(a, \hat{k}_{\text{inc}}, \hat{k}) = \vec{V}_{\text{obs}}^{\text{out}}(a, -\hat{k}_{\text{inc}}, \hat{k}). \quad (2.48)$$

Finally, one needs to calculate the amplification factor α in order to evaluate (2.47). The amplification factor relates the pattern resulting from the PO currents to the pattern of the actual field in the following way

$$\vec{V}_{\text{obs}}^{\text{in/out}} = \alpha \vec{V}_{\text{PO}}^{\text{in/out}}. \quad (2.49)$$

Recalling (2.33) and using (2.47) and (2.49)

$$\alpha = \frac{|E_0| A_{\text{eff,PO}}}{\lambda \left| \vec{V}_{\text{PO}}^{\text{out}}(a, \hat{k}_{\text{inc}}, \hat{k}) \right|_{\text{max}}} = \frac{|E_0| A_{\text{eff,PO}}}{\lambda \frac{k |E_0| a^2}{2}} = \frac{|E_0| A_{\text{eff,PO}}}{\lambda \frac{|E_0| \pi a^2}{\lambda}} = \frac{A_{\text{eff,PO}}}{A_{\text{ph}}} \quad (2.50)$$

which is the ratio between the effective area $A_{\text{eff,PO}}$ and the physical area A_{ph} as shown in [16]. The resulting amplification factor has been calculated for this type of structure and is shown in Fig. 2.7, where α is plotted versus the radius a . As it can be seen, for small structures $\alpha \rightarrow \infty$ to compensate for a vanishing antenna size. However, in the case of larger antenna sizes $\alpha \rightarrow 1$ due to the fact that the effective and physical area of the structure are similar.

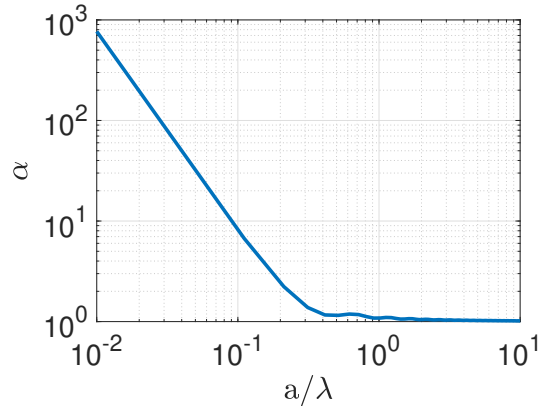


Figure 2.7: Amplification factor α for a spherical structure under plane wave incidence as a function of the radius in terms of wavelength.

In Fig. 2.8 the directivity of the observable field for three different sizes is presented. Furthermore, the directivity in the case of broadside incidence, i.e., $\theta_i = 0^\circ$, and scanning at $\theta_i = 60^\circ$ are considered. The maximum directivity remains constant when scanning, because the illuminated surface of the sphere is constant for any incidence. Furthermore, a higher directivity is associated with a larger size and thus cross-sectional area.

The maximum directivity calculated with the PO currents is compared with the one obtained with the spherical modes (2.22) in Fig. 2.9. When using the PO approach we can see that the observable field pattern is dependent on the geometry of the structure. Therefore, the power carried by the inward/outward observable field is continuous with respect to the size of the structure. This fact renders the effective area a continuous function, as can be seen from Fig. 2.9. In this figure it can be seen that for small structures the effective area as calculated using the PO approach converges to the effective area of Huygens' source. For larger apertures the effective area approaches the physical area of the structure as expected.

2.4.2 Rectangular Domain

As previously mentioned, the observable field has been thoroughly analyzed for spherical domains [16–18]. However, the concept of the observable field is extended also to planar domains, which are of more practical relevance, since planar antennas are the most common solution for massive MIMO applications. In this section we consider the observable field for rectangles having sides S_x and S_y along x and y , respectively, as shown in Fig. 2.10.

Differently from conformal domains, e.g., the case of the sphere treated in Subsec. 2.4.1, the observable field from a planar domain depends on the direction of incidence. This is because in the case of non-broadside incidence, the currents on the planar structure have a linear phase, leading to a reduction in directivity known as scan loss. This was not the case with the sphere since the portion of the structure illuminated by the plane wave was constant irrespective of the direction of incidence, thus giving rise to the same observable field. In the case of the planar domain the projected area is reduced when scanning as can be seen when Fig. 2.11b is compared to Fig. 2.11a.

Similar to the previous section, we consider a plane wave impinging from \vec{k}_{inc} with polarization \hat{p}_{inc} as follows

$$\vec{E}_{\text{inc}} = |E_0| e^{-j\vec{k}_{\text{inc}}\vec{r}'} \hat{p}_{\text{inc}}. \quad (2.51)$$

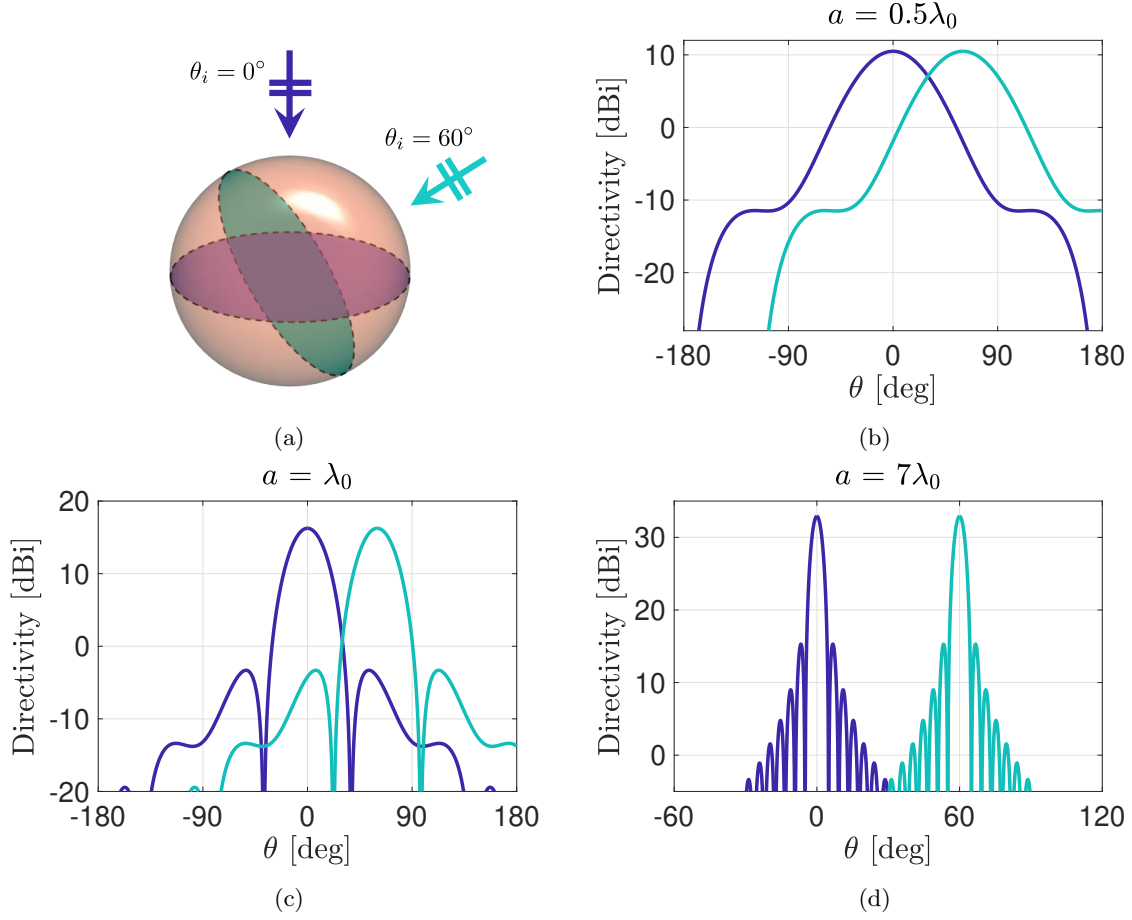


Figure 2.8: (a) Spherical domain of radius a illuminated by a TM plane wave impinging from $\theta_i = 0^\circ$ and $\theta_i = 60^\circ$, and the resulting directivity patterns for (b) $a = 0.5\lambda$, (c) $a = \lambda$ and (d) $a = 7\lambda$.

Therefore, the radiation integrals in (2.39) can be written as

$$\vec{E}_{\text{obs}}^{\text{out}}(\vec{r}) = jk\alpha|E_0|\frac{e^{-jkr}}{4\pi r}\iint_S e^{-j\vec{k}_{\text{inc}}\vec{r}'}e^{j\vec{k}\vec{r}'}d\vec{r}'\left[\left(\underline{\underline{I}}-\hat{r}\hat{r}\right)\cdot\hat{n}\times\left(\hat{k}_{\text{inc}}\times\hat{p}_{\text{inc}}\right)-\hat{r}\times\left(\hat{n}\times\hat{p}_{\text{inc}}\right)\right]. \quad (2.52)$$

The integral in (2.52) can be solved by writing the exponent in cartesian coordinates as follows

$$\iint_S e^{-j\vec{k}_{\text{inc}}\vec{r}'}e^{j\vec{k}\vec{r}'}d\vec{r}' = \int_{-S_x/2}^{S_x/2} e^{j(k_x-k_{\text{inc},x})x'}dx'\int_{-S_y/2}^{S_y/2} e^{j(k_y-k_{\text{inc},y})y'}dy' \quad (2.53)$$

For which the analytical solution is as follows

$$\iint_S e^{-j\vec{k}_{\text{inc}}\vec{r}'}e^{j\vec{k}\vec{r}'}d\vec{r}' = S_x\text{sinc}\left(\frac{S_x(k_x-k_{\text{inc},x})}{2}\right)S_y\text{sinc}\left(\frac{S_y(k_y-k_{\text{inc},y})}{2}\right). \quad (2.54)$$

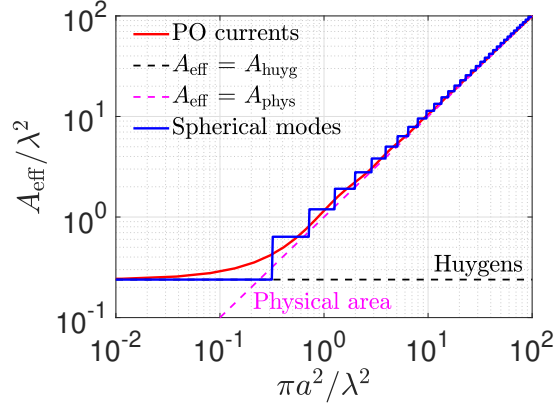


Figure 2.9: Maximum effective area of a spherical domain of radius a calculated using the the spherical modes and the PO currents, compared with the physical area of the domain, and the effective area of a Huygens source.

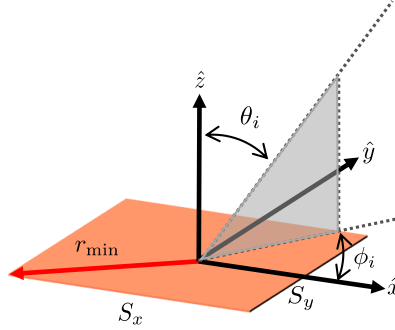


Figure 2.10: Planar rectangular structure considered in Subsec. 2.4.2.

Hence, the outward observable field has the following pattern

$$\vec{V}_{\text{obs}}^{\text{out}}(\hat{k}_{\text{inc}}, \hat{k}) = \frac{jk\alpha|E_0|}{4\pi} S_x \text{sinc}\left(\frac{S_x(k_x - k_{\text{inc},x})}{2}\right) S_y \text{sinc}\left(\frac{S_y(k_y - k_{\text{inc},y})}{2}\right) \left[(\underline{\underline{I}} - \hat{r}\hat{r}) \cdot \hat{n} \times (\hat{k}_{\text{inc}} \times \hat{p}_{\text{inc}}) - \hat{r} \times (\hat{n} \times \hat{p}_{\text{inc}}) \right]. \quad (2.55)$$

The pattern of the inward observable field is then given by the following expression

$$\vec{V}_{\text{obs}}^{\text{inw}}(\hat{k}_{\text{inc}}, \hat{k}) = \frac{jk\alpha|E_0|}{4\pi} S_x \text{sinc}\left(\frac{S_x(k_x + k_{\text{inc},x})}{2}\right) S_y \text{sinc}\left(\frac{S_y(k_y + k_{\text{inc},y})}{2}\right) \left[(\underline{\underline{I}} - \hat{r}\hat{r}) \cdot \hat{n} \times (\hat{k}_{\text{inc}} \times \hat{p}_{\text{inc}}) - \hat{r} \times (\hat{n} \times \hat{p}_{\text{inc}}) \right]. \quad (2.56)$$

A more extensive derivation of the observable field for a rectangular plate can be found in Appendix B.

To calculate the amplification factor α , the maximum of the PO pattern needs to be calculated, where we recall that the PO pattern and the observable field pattern have the following relationship

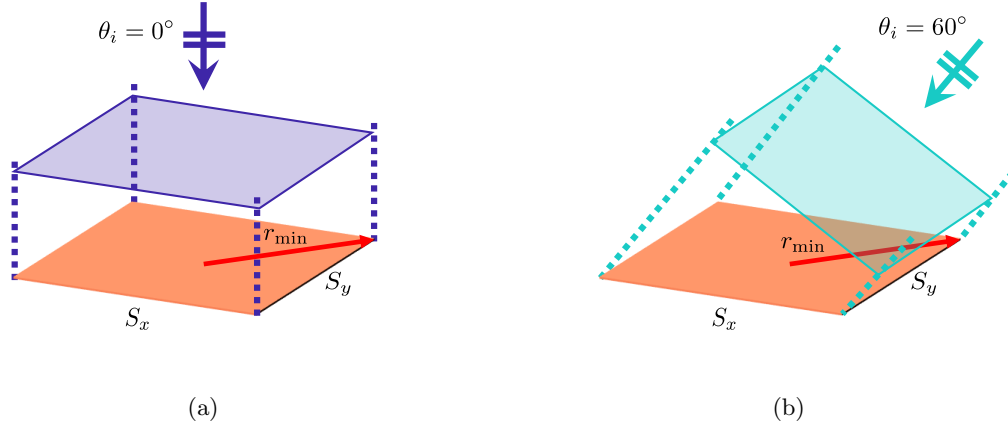


Figure 2.11: Structure under analysis in the case of (a) a plane wave impinging from broadside and (b) a plane wave impinging from $\theta_i = 60^\circ$ with reduced projected area.

$$\vec{V}_{\text{obs}} = \alpha \vec{V}_{\text{PO}}. \quad (2.57)$$

The evaluation of α is done numerically, since the maximum of (2.56) depends on the size of the structure. For smaller structures the maximum is dominated by the vectorial part, for which the maximum occurs in the direction of the normal to the structure. In the case of large structures the maximum is dominated by the directive pattern and thus occurs when the direction of observation coincides with the direction of incidence of the plane wave as seen by the structure, or mathematically $\hat{k} = -\hat{k}_{\text{inc}}$. In this latter case, the PO pattern attains a maximum value given by

$$\left| \vec{V}_{\text{PO}}^{\text{out}}(\hat{k}_{\text{inc}}, \hat{k}) \right|_{\text{max}} = \left| \vec{V}_{\text{PO}}^{\text{out}}(\hat{k}_{\text{inc}}, -\hat{k}_{\text{inc}}) \right| = \frac{k|E_0|}{4\pi} S_x S_y 2 \cos \theta_i = \frac{k|E_0|}{2\pi} A_{\text{ph}} \cos \theta_i. \quad (2.58)$$

Where A_{ph} is the physical area of the structure. By using (2.33) we find

$$\alpha = \frac{|E_0| A_{\text{eff,PO}}}{\lambda \left| \vec{V}_{\text{PO}}^{\text{out}}(\hat{k}_{\text{inc}}, \hat{k}) \right|_{\text{max}}} = \frac{|E_0| A_{\text{eff,PO}}}{\lambda \frac{k|E_0|}{2\pi} A_{\text{ph}} \cos \theta_i} = \frac{A_{\text{eff,PO}}}{A_{\text{ph}} \cos \theta_i}. \quad (2.59)$$

It can be seen that the amplification factor α in the case of a rectangular structure is similar to the previously found α for the sphere. However, in the case of the rectangular structure we see the effect of a reduction in the projected area due to a skewed angle of incidence, where the physical area is multiplied by $\cos \theta_i$. The result for the amplification factor in the case of a plane wave impinging from broadside is shown in Fig. 2.12. As expected, for small structures $\alpha \rightarrow \infty$ to compensate for a vanishing antenna size. However, in the case of larger antenna sizes $\alpha \rightarrow 1$ due to the fact that the effective and physical area of the structure are similar.

In Fig. 2.13 the directivity results for a rectangular structure enveloped by a sphere of radius r_{\min} , as in Fig. 2.8a, are shown. The structure under analysis is considered in the case of a plane wave impinging from broadside (i.e., $\theta_i = 0^\circ$) and for a plane wave impinging from $\theta_i = 60^\circ$ and $\phi = 0^\circ$ for three different r_{\min} : an electrically small structure, i.e., $r_{\min} = 0.5\lambda$, in Fig. 2.13b, a medium-sized structure $r_{\min} = \lambda$ in Fig. 2.13c, and an electrically large structure $r_{\min} = 7\lambda$ in Fig. 2.13d. Furthermore, a comparison is made between the directivity in the case of the rectangular structure and its enveloping sphere. As can be seen from Fig. 2.13 for all structure sizes, the directivity of the rectangular plate is smaller than the one of the sphere, due to a smaller area. In fact, the physical area of the plate is smaller by a factor $\pi/2$ than and the cross section of its enveloping

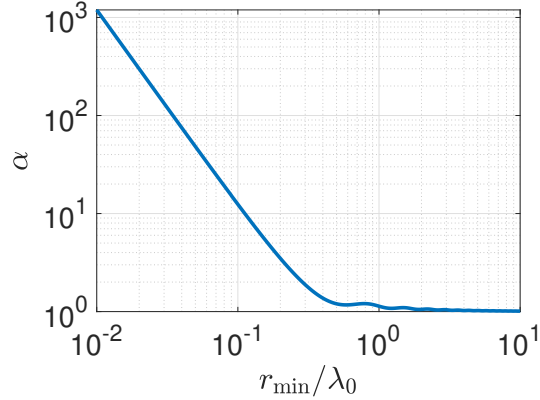


Figure 2.12: Amplification factor α for a rectangular structure under plane wave incidence as a function of the radius of the enveloping sphere in terms of wavelength.

sphere. Therefore, the directivity achieved by the sphere is larger. For electrically small plates, the scanning causes an aberration in the patterns, giving rise to a maximum directivity which does not coincide with the direction of the impinging plane wave, this can be seen in Fig. 2.13b and Fig. 2.13c, where the maximum of radiation occurs for smaller angles than the expected 60° . Moreover, the scan loss effect is less detrimental for smaller structure due to their non-directive patterns. However, in the case of larger structures, the maximum radiation is asymptotic to $\cos \theta_i$. This effect is clarified in Fig. 2.14, where the directivity of a square plate of size $r_{\min} = 7\lambda$ for plane waves impinging from $\theta_i = 0^\circ$ and $\theta_i = 60^\circ$, as in Fig. 2.13d, are compared with $\cos \theta$ weighted by the maximum directivity at broadside. As can be seen the maxima follow the trace of the cosine, since the reduction in area is proportional to $\cos \theta_i$.

An important clarifying consideration is that only patterns in the $\phi = 0^\circ$ plane are shown. This is sufficient, since the structure considered is symmetric and both magnetic and electric currents are used to construct the observable field.

2.4.3 Planar Circular Domain

In this section a planar circular structure is considered. This has applications in the case of circular arrays [25]. In contrast with the sphere where its observable field was calculated using the cross-sectional disk, in this case we consider an irrotational disk. This means that similar to the rectangular plate of Subsec. 2.4.2, the structure introduces scan loss when scanning.

The pattern of the observable field in the case of sphere was derived in Subsec. 2.4.1. In that subsection we assumed a cross-sectional disk, always perpendicular to the direction of incidence of the incoming plane wave. This causes a constant phase across the structures. However, in this case, the currents that arise from an incoming plane wave may have a linear phase along the structure.

As previously, we consider a plane wave impinging from \vec{k}_{inc} with polarization \hat{p}_{inc} as follows

$$\vec{E}_{\text{inc}} = |E_0| e^{-j\vec{k}_{\text{inc}}\vec{r}'} \hat{p}_{\text{inc}}. \quad (2.60)$$

Therefore, the radiation integrals in (2.39) can be written as

$$\vec{E}_{\text{obs}}^{\text{out}}(\vec{r}) = jk\alpha |E_0| \frac{e^{-jk r}}{4\pi r} \iint_D e^{-j\vec{k}_{\text{inc}}\vec{r}'} e^{j\vec{k}\vec{r}'} d\vec{r}' \left[(\underline{\underline{I}} - \hat{r}\hat{r}) \cdot \hat{n} \times (\hat{k}_{\text{inc}} \times \hat{p}_{\text{inc}}) - \hat{r} \times (\hat{n} \times \hat{p}_{\text{inc}}) \right]. \quad (2.61)$$

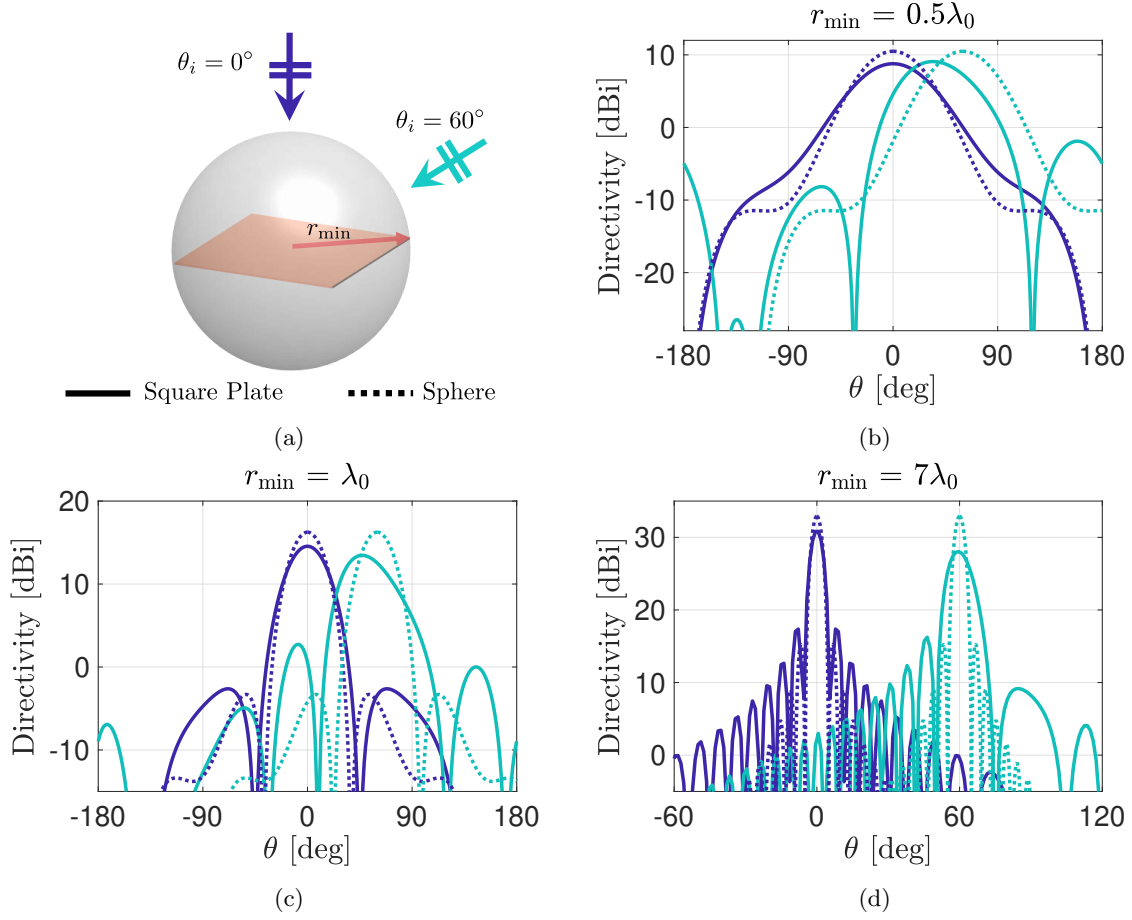


Figure 2.13: (a) Rectangular domain of size r_{\min} illuminated by a plane wave impinging from $\theta_i = 0^\circ$ and $\theta_i = 60^\circ$, and the resulting directivity patterns for (b) $r_{\min} = 0.5\lambda$, (c) $r_{\min} = \lambda$ and (d) $r_{\min} = 7\lambda$.

Where D is a disk with radius r_{\min} located on the xy -plane, as shown in Fig. 2.15. Recalling that the pattern of the inward observable field is related to the pattern of the outward observable field in the following way

$$\vec{V}_{\text{obs}}^{\text{inw}}(\hat{k}_{\text{inc}}, \hat{k}) = \vec{V}_{\text{obs}}^{\text{out}}(-\hat{k}_{\text{inc}}, \hat{k}) \quad (2.62)$$

and by writing the structure's coordinates, \vec{r}' , in polar coordinates the integral in (2.61), can be written as follows

$$\iint_D e^{j\vec{k}_{\text{inc}}\vec{r}'} e^{j\vec{k}\vec{r}'} d\vec{r}' = \int_0^a \int_0^{2\pi} e^{-jk\rho' \sin\theta_i \cos(\phi' - \phi_i)} e^{jk\rho' \sin\theta \cos(\phi' - \phi)} d\phi' \rho' d\rho' \quad (2.63)$$

where the radius of the enveloping sphere is taken as a . The integral in (2.63) is calculated analytically

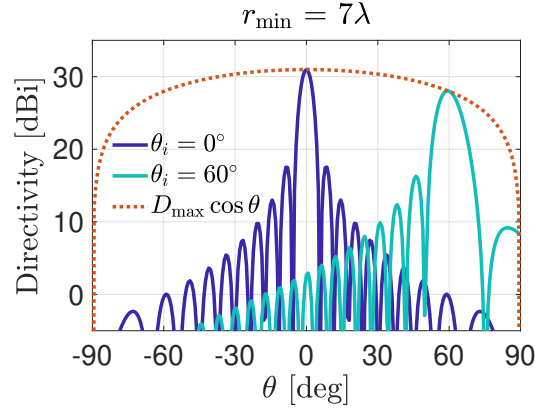


Figure 2.14: Directivity of the observable field in the case of square plate characterized by $r_{\min} = 7\lambda$, for the case of a plane wave impinging from $\theta_i = 0^\circ$ and $\theta_i = 60^\circ$, compared with a cosine weighted by the maximum directivity in the case of broadside incidence.

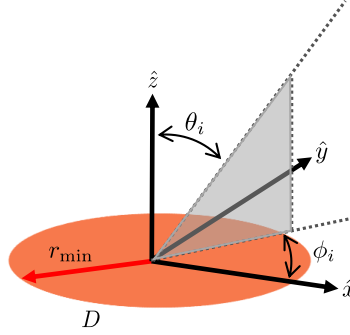


Figure 2.15: Planar circular structure considered in Subsec. 2.4.3.

ically in Appendix C, and it results into the following expression

$$\iint_D e^{j\vec{k}_{\text{inc}}\vec{r}'} e^{j\vec{k}\vec{r}'} d\vec{r}' = 2\pi a \frac{\sin\theta_i J_1(ka\sin\theta_i)J_0(ka\sin\theta) - \sin\theta J_0(ka\sin\theta_i)J_1(ka\sin\theta)}{k(\sin^2\theta_i - \sin^2\theta)} +$$

$$+ 4\pi a \sum_{n=1}^{\infty} \cos(n(\phi - \phi_i)) \frac{\sin\theta J_n(ka\sin\theta_i)J_{n-1}(ka\sin\theta) - \sin\theta_i J_{n-1}(ka\sin\theta_i)J_n(ka\sin\theta)}{k(\sin^2\theta_i - \sin^2\theta)}. \quad (2.64)$$

The infinite sum in (2.64) is truncated at $N = \lceil ka \rceil$. The radiated field calculated using (2.64) is validated by a comparison with a numerical evaluation of the integral, implemented by discretizing the disk into square patches. In Fig. 2.16 the analytical solution is compared to the numerical one, for a plane wave impinging from $\theta_i = 60^\circ$ for $r_{\min} = 0.5\lambda$ in Fig. 2.16a and for $r_{\min} = 7\lambda$ Fig. 2.16b. The calculation of the amplification factor α for a planar disk is similar to previous sections by using (2.33) in which the evaluation of the maximum value of the PO pattern is implemented numerically. The results of the amplification factor can be seen in Fig. 2.17. As expected, for small structures $\alpha \rightarrow \infty$ to compensate for a vanishing antenna size. However, in the case of larger antenna sizes $\alpha \rightarrow 1$ due to the fact that the effective and physical area of the structure are similar.

The directivity of the disk is shown in Fig. 2.18 for a plane wave impinging from broadside and

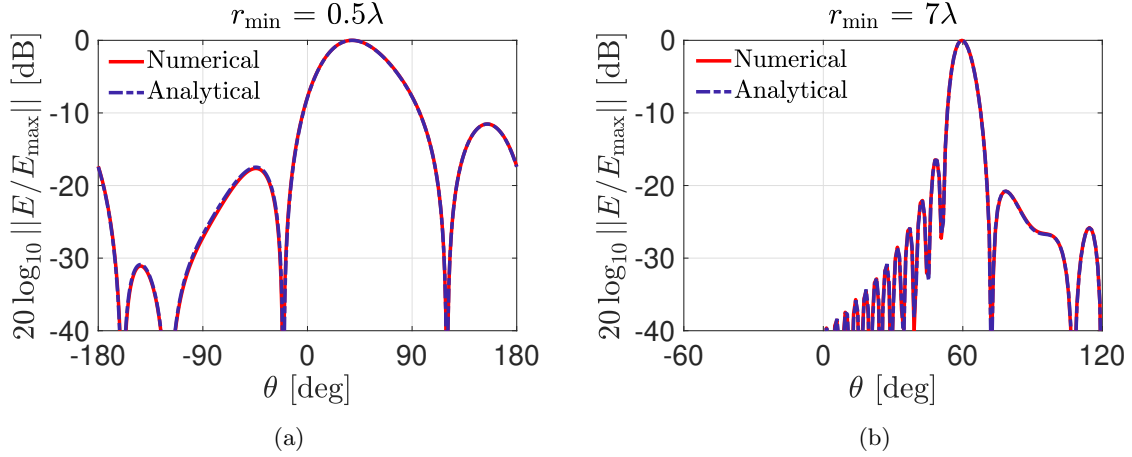


Figure 2.16: Validation of analytical implementation of the observable field pattern with numerical results in the case of a plane wave impinging from $\theta_i = 60^\circ$ for structures of size (a) $r_{\min} = 0.5\lambda$ and (b) $r_{\min} = 7\lambda$.

from $\theta_i = 60^\circ$ [see Fig. 2.18(a)] for three different electrical sizes, i.e., $r_{\min} = 0.5\lambda_0$ in Fig. 2.18(b), $r_{\min} = \lambda_0$ in Fig. 2.18(c), and $r_{\min} = 7\lambda$ in Fig. 2.18(d). For the broadside incidence the directivity of the disk is the same as the one of the sphere, because the observable field from the sphere is calculated with the cross-sectional disk. However, when scanning, the planarity of the structure introduces an aberration in the pattern causing the maximum to be located closer to broadside and not the direction of incidence of the plane wave. For larger structure as in Fig. 2.18d, the maxima of the directivity traces a cosine pattern, due to the scaling of the projected area when scanning, as discussed in Subsec. 2.4.2.

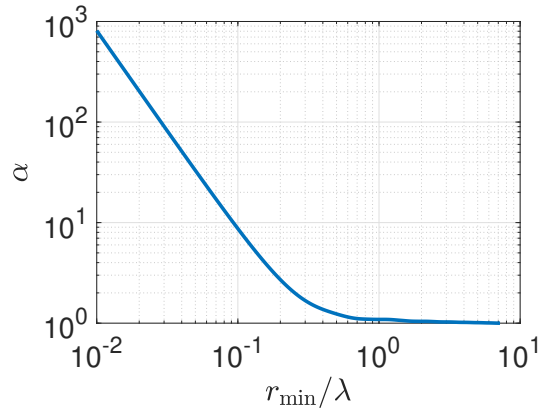


Figure 2.17: Amplification factor α for a planar circular structure under plane wave incidence as a function of the radius of the enveloping sphere in terms of wavelength.

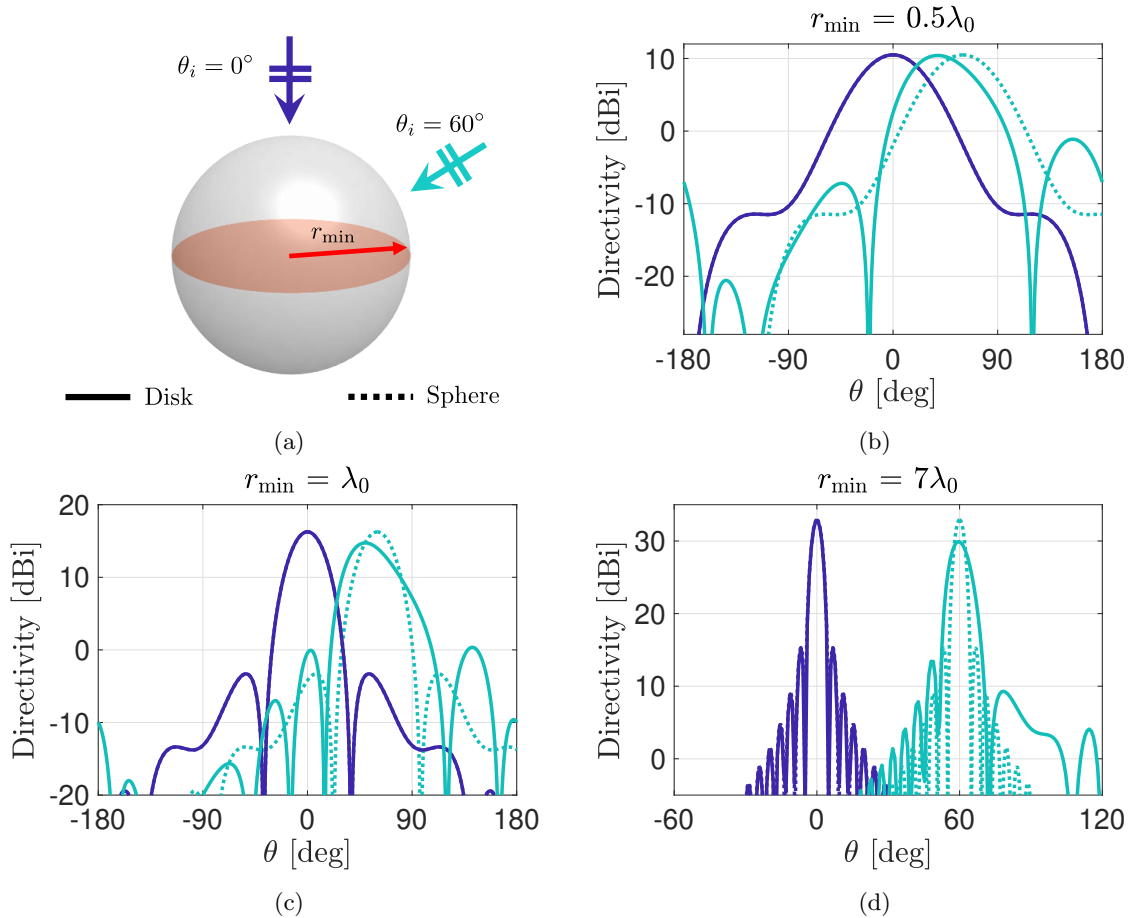


Figure 2.18: (a) Planar circular domain of radius r_{\min} illuminated by a plane wave impinging from $\theta_i = 0^\circ$ and $\theta_i = 60^\circ$, and the resulting directivity patterns for (b) $r_{\min} = 0.5\lambda$, (c) $r_{\min} = \lambda$ and (d) $r_{\min} = 7\lambda$.

This Page Intentionally Left Blank

3. Number of Beams Analysis

As mentioned in the introduction the goal of this study is to investigate the maximum number of independent beams that can be hosted by a given platform. This depends on the physical size of the structure. In order to characterize the independence of the beams we accept a given level of Signal to Interference Ratio (SIR). This chapter demonstrates the methodology used to calculate the SIR by resorting to the concept of the observable field and introduces the coupling coefficients to calculate the power available to the antenna under analysis.

3.1 Coupling Coefficients

In a multi-link communication scenario, for a given link its data stream represents the desired signal while all other data streams contribute to the interference. In order to consider a given link independent of others, the SIR must remain above a certain threshold. To model the SIR of a given link in a communication scenario we need to characterize the power received from each client. In this context, the observable field is used together with the coupling coefficients to calculate the power that an antenna with a given radiation pattern can receive from an incident field.

Consider an antenna enclosed by a sphere of radius a , with its j -th beam \vec{V}_a^j pointing to the \hat{k}_j direction. Assume a client located in the antenna far field, generating a plane wave impinging from the direction \hat{k}_i . To calculate the power P_{rec}^{ij} that can be received from a source located at the direction \hat{k}_i , when the antenna is pointing to the \hat{k}_j direction, we can define the reception coupling coefficient as follows

$$P_{\text{rec}}^{ij} \equiv P_{\text{obs}}^i |C_{\text{obs},a}^{ij}|^2 \quad (3.1)$$

where $C_{\text{obs},a}^{ij}$ is the coupling between the observable field pattern $\vec{V}_{\text{obs},i}^{\text{inw}}(\hat{k})$, carrying the observable power P_{obs}^i , associated with the plane wave impinging from \hat{k}_i , and the antenna pattern $\vec{V}_a^j(\hat{k})$ pointing to direction \hat{k}_j , as summarized in Fig. 3.1. To calculate the coupling coefficient $C_{\text{obs},a}^{ij}$, the power received can be related to the open circuit voltage induced on the terminals of the antenna and the input current by which the antenna would be fed in transmission. We can write the power received from the i -th client when pointing to the j -th direction under impedance matched conditions in the following way

$$P_{\text{rec}}^{ij} = \frac{1}{8} \frac{|V_{\text{oc}}^{ij}|^2}{R_a^j} \quad (3.2)$$

where V_{oc}^{ij} is the open circuit voltage induced in the terminals of the antenna by the i -th impinging field and R_a^j is the radiation resistance when pointing to the j -th direction. As suggested in [26], the power received can be related to the power radiated by the antenna when operated in transmission in the following way

$$P_{\text{rec}}^{ij} = \frac{P_r^{ij} P_a^j}{P_a^j} = \frac{1}{8} \frac{|V_{\text{oc}}^{ij}|^2}{R_a^j} \frac{1}{2} \frac{R_a^j |I_a^j|^2}{P_a^j} = \frac{1}{16} \frac{|V_{\text{oc}}^{ij} I_a^j|^2}{P_a^j} \quad (3.3)$$

where P_a^j is the power radiated by the antenna in transmission when fed by a current I_a^j . By using (3.1) and (3.3) the coupling coefficients can be calculated as follows

$$|C_{\text{obs},a}^{ij}| = \frac{|V_{\text{oc}}^{ij} I_a^j|}{4 \sqrt{P_a^j P_{\text{obs}}^i}}. \quad (3.4)$$

The product $V_{\text{oc}}^{ij} I_a^j$ can be evaluated by exploiting Lorentz's reciprocity theorem, which in the case of a source at a far field distance can be simplified as follows

$$V_{\text{oc}}^{ij} I_a^j = \frac{2}{\zeta} \iint_{4\pi} \vec{V}_{\text{obs},i}^{\text{inw}}(\hat{k}) \cdot \vec{V}_a^j(\hat{k}) d\hat{k}. \quad (3.5)$$

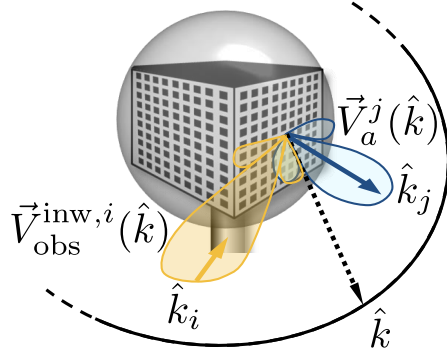


Figure 3.1: Antenna pattern with an inward observable field pattern.

Furthermore, the power radiated by the transmitting antenna and the observable power can also be related to their patterns in the following way

$$P_{\text{obs}}^i = \frac{1}{2\zeta} \iint_{4\pi} |\vec{V}_{\text{obs}}^{\text{inw},i}(\hat{k})|^2 d\hat{k} \quad (3.6)$$

$$P_a^j = \frac{1}{2\zeta} \iint_{4\pi} |\vec{V}_a^j(\hat{k})|^2 d\hat{k}. \quad (3.7)$$

Hence, the coupling coefficients can be written as

$$C_{\text{obs},a}^{ij} = \frac{\iint_{4\pi} \vec{V}_{\text{obs}}^{\text{inw},i}(\hat{k}) \cdot \vec{V}_a^j(\hat{k}) d\hat{k}}{\sqrt{\iint_{4\pi} |\vec{V}_{\text{obs}}^{\text{inw},i}(\hat{k})|^2 d\hat{k} \iint_{4\pi} |\vec{V}_a^j(\hat{k})|^2 d\hat{k}}}. \quad (3.8)$$

The maximum coupling, i.e., $|C_{\text{obs},a}^{ij}| = 1$, occurs when the pattern of the receiving antenna matches the pattern of the observable field, $\vec{V}_{\text{obs}}^{\text{inw},i}(\hat{k}) = \vec{V}_a^j(\hat{k})$. In this case the received power is maximized, however, this does not guarantee an optimum SIR as will be clarified in Chapter 4.

In Fig. 3.2 the power available, calculated as in (3.1), for rectangular structures of different sizes is presented. The simulation considers TM plane waves impinging from θ_i and the frequency of analysis is 100 GHz. As clarified in Fig. 3.2a two scanning directions are considered, for the case of scanning at $\theta = 0^\circ$ and $\theta = 60^\circ$. In the case of small structures as in Fig. 3.2b the power available from the desired scanning direction is not reduced since the structure is small in terms of wavelength and therefore has a broad antenna pattern. In the case of larger structure it can be seen from Fig. 3.2c and Fig. 3.2d that the power available from the scanning direction is reduced due to the scan loss. In previous works when spherical structures were considered as in [17], the power available from the scanning direction was not reduced with respect to broadside, since no scan loss was present.

3.1.1 Integration on the Far Field Sphere

In a given multi-link scenario, as the one shown in Fig. 1.1 where N_l clients are transmitting simultaneously, the analysis of the SIR when the antenna is pointing in the j -th direction to the desired user requires the calculation of the coupling coefficient as in (3.8) for each interferer i . This calculation must be repeated for every pointing direction j and possibly every antenna size in order

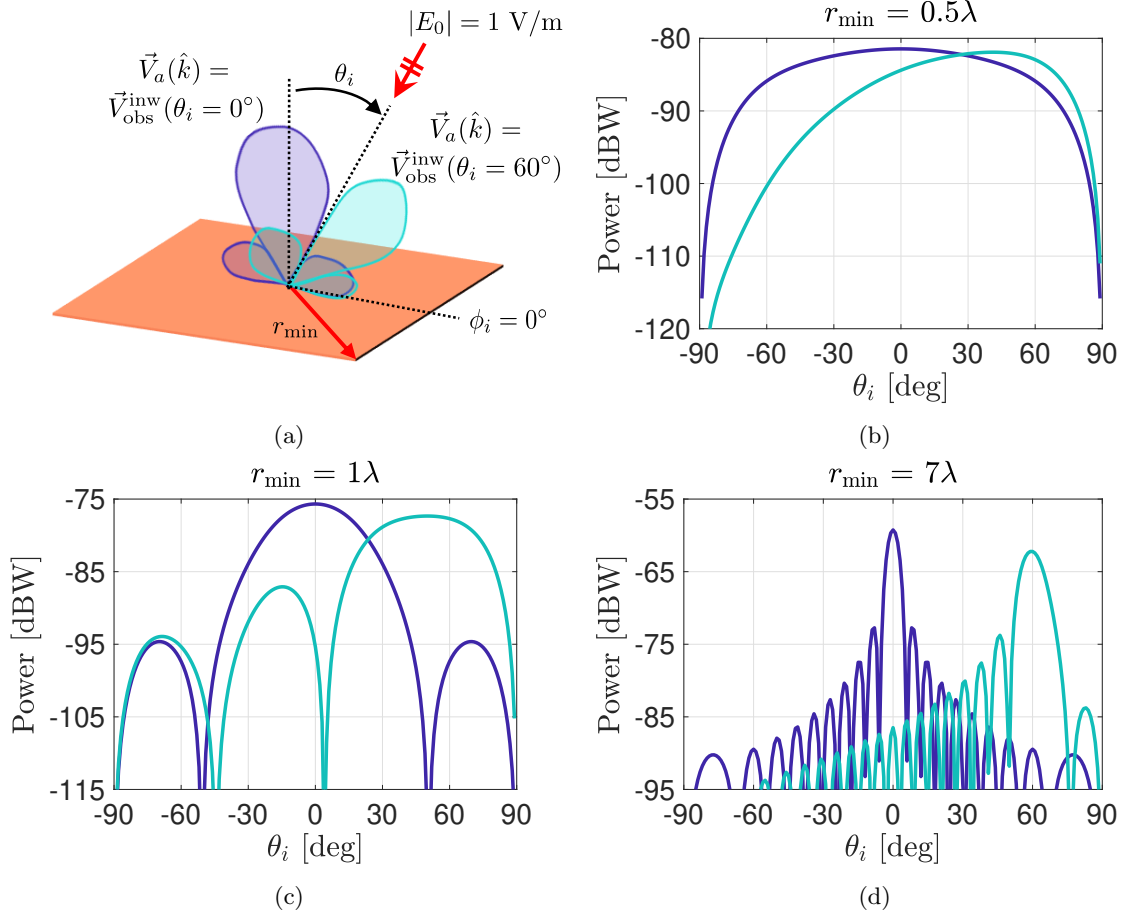


Figure 3.2: Power available in the case of TM plane waves impinging from θ_i for a (a) planar square domain while the antenna is pointing to $\theta = 0^\circ$ and $\theta = 60^\circ$ for the following sizes: (b) $r_{\text{min}} = 0.5\lambda$, (c) $r_{\text{min}} = \lambda$ and (d) $r_{\text{min}} = 7\lambda$.

to characterize the given scenario. Each evaluation of the coupling coefficient requires the calculation of multiple integrals, rendering this a computationally intensive problem. This subsection introduces the Gauss - Legendre quadrature rule as an aid to accelerate the calculation of such integrals.

The integrals considered in this case can be seen as integrals evaluated on the surface of the unit sphere \mathbb{S}^2 . As an example consider the power radiated by the antenna as in (3.7). In many cases the solution to such an integral might not be known analytically and thus must be computed numerically. It is therefore important to calculate an accurate approximation to the integrals of this form. A common way to approximate such an integral numerically is by the finite sum of weighted points on the sphere's surface \mathbb{S}^2 as follows

$$\int_{\mathbb{S}^2} f(\mathbf{x}) d\Omega \approx \sum_{i=0}^{N-1} w_i f(\mathbf{x}_i) \quad (3.9)$$

where w_i are the weights used in the type of quadrature. Before discussing a type of quadrature it

is important to recall the following property

$$\int_{\mathbb{S}^2} |f(\mathbf{x})|^2 d\Omega < \infty. \quad (3.10)$$

Functions for which (3.10) is valid are called square-integrable functions. As clarified in [27], square-integrable function on the unit sphere can be expanded in terms of the spherical harmonics orthonormal basis on the unit sphere. For which the spherical harmonical functions are given as follows

$$Y_n^m(\theta, \phi) = \frac{1}{\sqrt{2\pi}} P_n^m(\cos \theta) e^{jm\phi}, \quad -n \leq m \leq n, \quad n, m \in \mathbb{N} \quad (3.11)$$

where P_n^m are the normalised associated Legendre functions, m is the order of the spherical harmonic and n the degree. Integrating such a function would require solving the following integral

$$\int_{\mathbb{S}^2} e^{jm\phi} P_n^m(\cos \theta) \sin \theta d\theta d\phi. \quad (3.12)$$

Using Fubini's theorem the integral can be analyzed separately as

$$\int_0^{2\pi} e^{jm\phi} d\phi \quad (3.13)$$

and

$$\int_0^\pi P_n^m(\cos \theta) \sin \theta d\theta. \quad (3.14)$$

As explained in [28, 29], the optimal sample points for (3.13) consists of $L + 1$ equally spaced points, whereas for (3.14) the optimum sampling is using $(L + 1)/2$ Gauss - Legendre points. This ensures the exact integration of all Y_n^m for $-n \leq m \leq n$, $0 \leq n \leq L$. Recalling that the Gauss - Legendre scheme guarantees the exact integration of all polynomials $p_l(x)$ up until degree $l = 2n - 1$ over the interval $[-1, 1]$ as follows

$$\int_{-1}^1 p_l(x) dx = \sum_{i=1}^n w_i p_l(x_i) \quad (3.15)$$

with w_i the quadrature weights and x_i the nodes, which are the roots of the n -th Legendre polynomial. Hence, in order to employ a uniform sampling scheme along ϕ and Gauss - Legendre on θ the integrals as in (3.7) can be rewritten as follows

$$P_a^j = \frac{1}{2\zeta} \iint_{4\pi} |\vec{V}_a^j(\hat{k})|^2 d\hat{k} = \frac{1}{2\zeta} \int_0^{2\pi} \int_0^\pi |\vec{V}_a^j(\theta, \phi)|^2 \sin \theta d\theta d\phi \quad (3.16)$$

and introducing a change of variables $\gamma = \cos \theta$, $d\gamma = \sin \theta d\theta$ allows us to evaluate the integral as follows

$$P_a^j = \frac{1}{2\zeta} \int_0^{2\pi} \int_{-1}^1 |\vec{V}_a^j(\arccos(\gamma), \phi)|^2 d\gamma d\phi = \frac{1}{2\zeta} w^\phi \sum_{j=1}^{N_\phi} \sum_{i=1}^{N_\theta} w_i^\theta |\vec{V}_a^j(\arccos(\gamma_i), \phi_j)|^2 \quad (3.17)$$

with γ_i the Gauss nodes, w_i^θ Gauss - Legendre weights and

$$\begin{cases} \phi_j = \frac{2\pi(j-1)}{N_\phi} \\ w^\phi = \frac{2\pi}{N_\phi} \\ N_\phi = L + 1 \\ N_\theta = \frac{L+1}{2}. \end{cases} \quad (3.18)$$

For the case of a structure enveloped by a sphere with minimum diameter D , the number of spherical harmonics L needed is as follows

$$L = \lceil kD + 1.8d_0^{2/3}(kD)^{1/3} \rceil \quad (3.19)$$

where d_0 is the number of valid decimal digits [28, 30]. The Gauss nodes γ_i can be found using the Newton - Raphson method for calculating the roots of the Legendre polynomials, whereas the weights w_j^θ can be calculated as follows [31, p. 887]

$$w_j^\theta = \frac{2}{(1 - \theta_i^2)[P_n'(\theta_i)]^2}. \quad (3.20)$$

In Fig. 3.3a the power carried by the inward component of the observable field is calculated using two different quadrature schemes for the case of a planar square structure with minimum enveloping sphere of radius $r_{\min} = 0.1\lambda$. The case of using a uniform sampling in ϕ and Gauss - Legendre in θ is compared to the case of the traditional uniform sampling in both dimensions θ, ϕ using the quadrature rule $\Delta\theta = \Delta\phi$. The power, calculated as in (3.6), is plotted as a function of the total number of points. In the case of using a Gauss - Legendre quadrature the parameter d_0 is varied to increase the total number of sampling points. Furthermore, the relative error with respect to the final value of the integral, calculated as follows

$$\epsilon_r = \frac{|I_{\text{final}} - I_i|}{|I_{\text{final}}|} \quad (3.21)$$

where I_{final} is the final value of the integral as in (3.6), is show in Fig. 3.3b for the case of a planar square structure with minimum enveloping sphere of radius $r_{\min} = 0.1\lambda$. As it can be seen from these figures, employing a Gauss - Legendre quadrature scheme has a clear advantage of using fewer points. This accelerates the calculation of each integral which in turn facilitates the analysis of the SIR. In the case of a structure with $r_{\min} = 0.1\lambda$ the calculation time to achieve a relative error of $\epsilon_r < 10^{-4}$ is 0.47s in the case of the sampling scheme $\Delta\theta = \Delta\phi$ and 0.021s in the case of a uniform sampling along ϕ and Gauss - Legendre along θ . These results are also shown in the case of a large structure in terms of wavelength characterized by a minimum enveloping sphere of radius $r_{\min} = 10\lambda$ in Fig. 3.3c and Fig. 3.3d.

3.2 Signal-to-Interference Ratio Modelling

As explained in Sec. 3.1, the coupling coefficients can be used to calculate the total power received when the antenna is pointing to direction j from all clients in a certain communication scenario as follows

$$P_{\text{rec}}^j = \sum_{i=1}^{N_l} P_{\text{obs}}^i |C_{\text{obs,a}}^{ij}|^2 \quad (3.22)$$

where N_l is the number of links present in the communication scenario. Using the definition of the coupling coefficients we can calculate the signal power. This is the power captured from the j -th direction when the antenna is pointing to the j -th direction. The signal power is then

$$S^j = P_{\text{obs}}^j |C_{\text{obs,a}}^{jj}|^2 \quad (3.23)$$

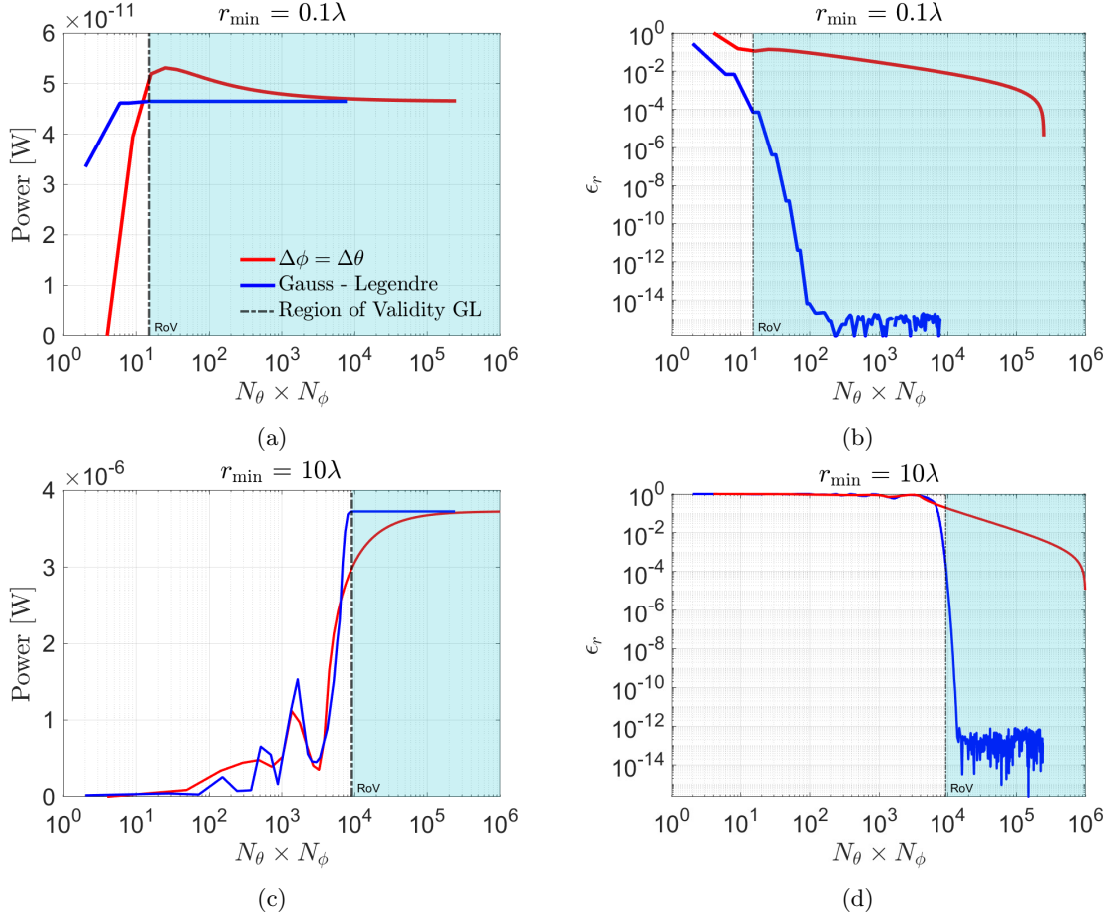


Figure 3.3: Power results from integration using two different quadrature schemes in the case of structures with size (a) $r_{\min} = 0.1\lambda$ and (b) their relative error, (c) power in the case of $r_{\min} = 10\lambda$ and (d) their relative error.

and thus the interference is the power contributed by the other clients, which is calculated as follows

$$I^j = \sum_{\substack{i=1 \\ i \neq j}}^{N_l} P_{\text{obs}}^i |C_{\text{obs},a}^{ij}|^2. \quad (3.24)$$

Using the signal and interference we can calculate the SIR of the communication scenario when the antenna is pointing to the j -th client as

$$\text{SIR}^j = \frac{S^j}{I^j} = \frac{P_{\text{obs}}^j |C_{\text{obs},a}^{jj}|^2}{\sum_{\substack{i=1 \\ i \neq j}}^{N_l} P_{\text{obs}}^i |C_{\text{obs},a}^{ij}|^2}. \quad (3.25)$$

In Fig. 3.4, a communication scenario consisting of three TM polarized plane waves impinging from $\theta_i = 0^\circ$, $\theta_i = 30^\circ$ and $\theta_i = 60^\circ$ is analyzed for the case of three different structures, when the antenna is pointing to broadside. The frequency considered for this analysis is of 100 GHz. In Fig. 3.4a a square plate is considered, in Fig. 3.4b a circular planar structure and in Fig. 3.4c a

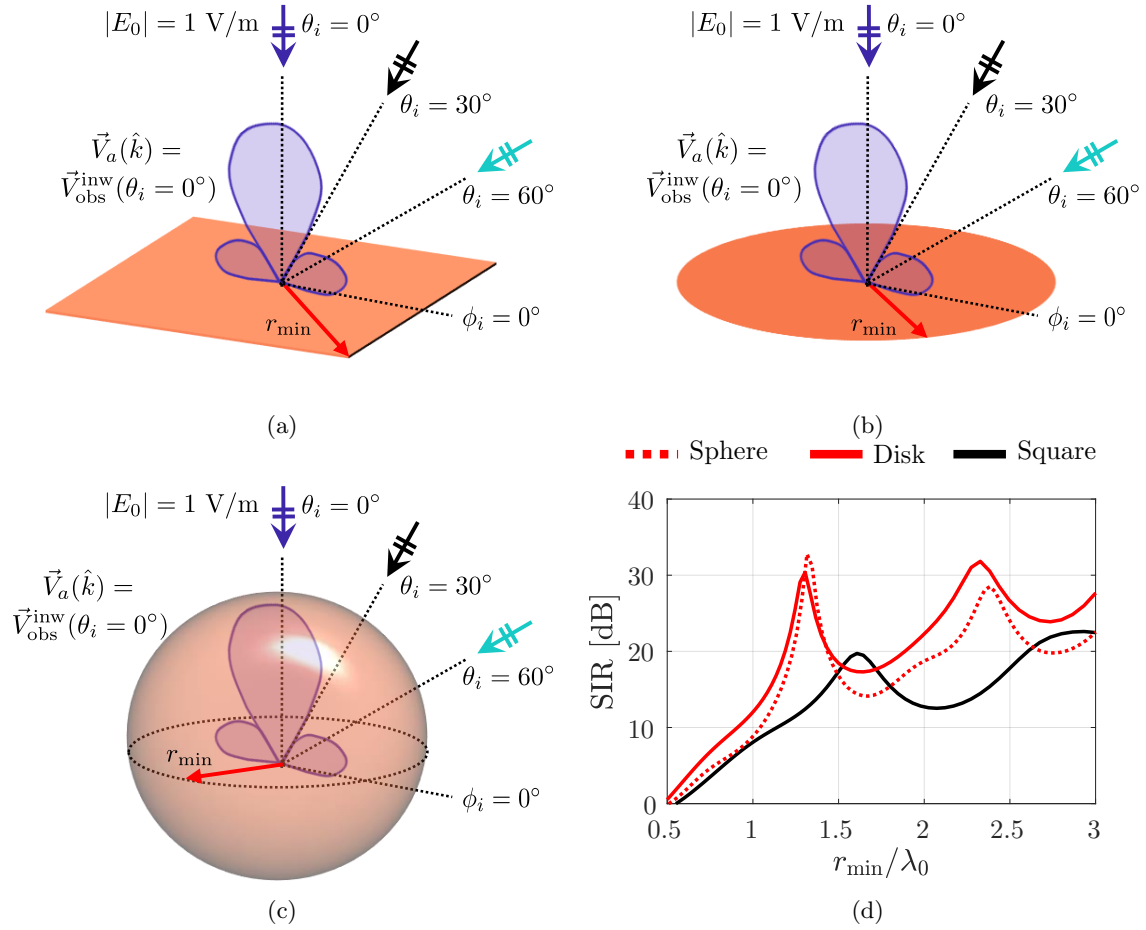


Figure 3.4: (a) Square structure, (b) circular planar structure, (c) spherical structure in the presence of three TM plane waves impinging from $\theta_i = 0^\circ$, $\theta_i = 30^\circ$ and $\theta_i = 60^\circ$ and (d) the SIR for each structure in case the antenna is pointing to broadside.

sphere. The resulting SIR versus the antenna size for all three structures is shown in Fig. 3.4d. In this analysis the antenna pattern \vec{V}_a^j is taken to be the one of the observable field \vec{V}_{obs}^j in the case of broadside. If the results of the sphere are compared to the disk it can be seen that they are similar, this is because the sphere was represented by a disk always perpendicular to the direction of incidence. The differences arise because of the scan loss present in the case of the disk but not in the case of the sphere. Therefore, the disk captures less interference while capturing the same signal power as the disk and hence improving the overall SIR. In the case of the square plate, the lower SIR can be attributed to the smaller aperture area. The maxima of the SIR occurs when the angle of incidence of a plane wave coincides with a null in the antenna pattern. This is clarified by the antenna pattern for the case of the sphere or the disk and the square plate in Fig.3.5a and Fig.3.5b, respectively, where the size is taken to be the one at the first maxima of the SIR in Fig. 3.4d. It can be seen that in both cases the nulls of the antenna pattern \vec{V}_a^j , chosen to be equal to the one of the observable field \vec{V}_{obs}^j , has nulls close to the angles of incidence of the interferers.

In Fig. 3.6a three TM plane waves are impinging on a square plate from $\theta_i = 0^\circ$, $\theta_i = 30^\circ$, and $\theta_i = 60^\circ$, and the resulting SIR is shown in Fig. 3.6b, when the antenna beam is pointing towards

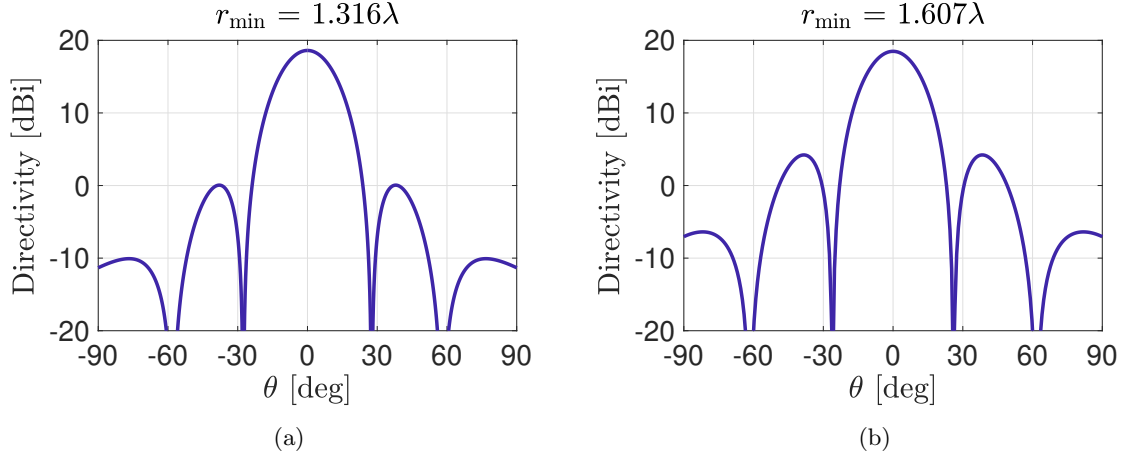


Figure 3.5: Directivity of antenna with size characterized by the minimum enveloping sphere with radius r_{\min} at the maximum SIR for (a) a sphere or disk pointing to broadside and (b) a square plate pointing to broadside.

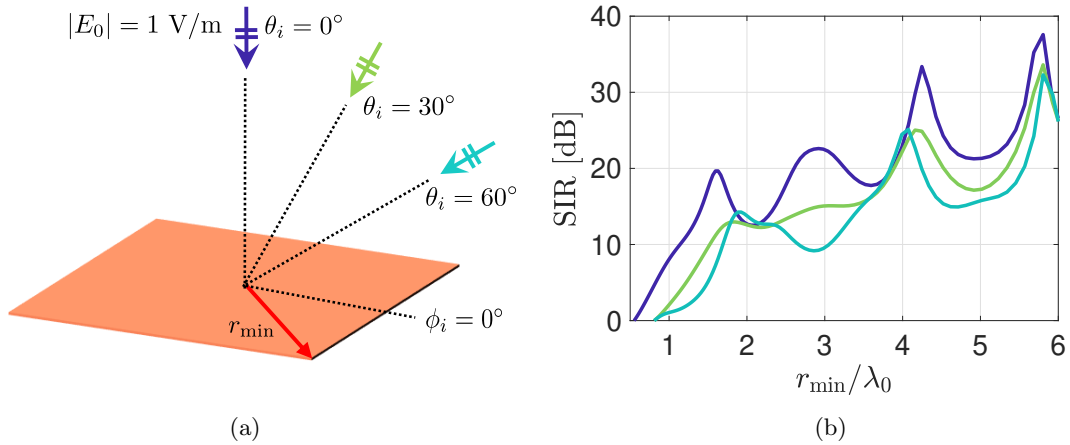


Figure 3.6: (a) Square plate, enveloped by a sphere having minimum radius r_{\min} in the presence of three TM plane waves impinging from $\theta_i = 0^\circ$, $\theta_i = 30^\circ$ and $\theta_i = 60^\circ$ and (b) the SIR evaluated when each plane wave is the signal and the remaining two are interferers.

0° , 30° , and 60° for a frequency of operation of 100 GHz. For each of these three cases, the signal is aligned with the antenna pattern, and the remaining two are interferers. When scanning, the SIR results to be deteriorated, also influenced by some aberrations in the patterns. In Fig. 3.7a a disk is considered in the same situation as the plate in Fig. 3.6a. The SIR corresponding to the disk is presented in Fig. 3.7b, similar as in the case of the square plate, the SIR is deteriorated when scanning.

3.3 Randomly Distributed Clients

In a realistic communication scenario the users will not be located equispaced of each other. Furthermore, antenna's scanning are limited to a certain Field of View (FoV). This section evaluates

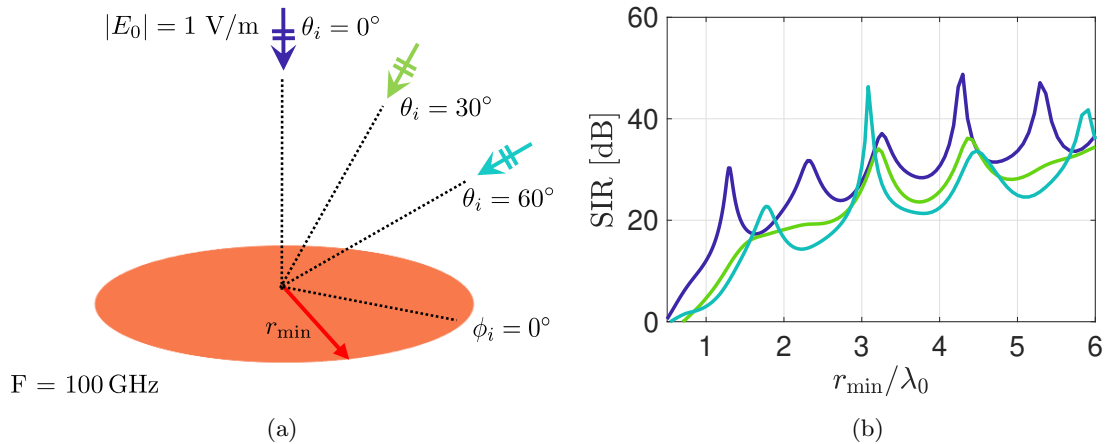


Figure 3.7: (a) Disk of radius r_{\min} in the presence of three TM plane waves impinging from $\theta_i = 0^\circ$, $\theta_i = 30^\circ$ and $\theta_i = 60^\circ$ and (b) the SIR evaluated when each plane wave is the signal and the remaining two are interferers.

the SIR performance for an antenna with a FoV of 120° . The FoV is divided equally in angular sectors $\Delta\theta$ in which each interferer can be located. The desired signal is limited to be located within $\Delta\theta/2$, around broadside, since otherwise the desired signal's location and an interferer's location could overlap rendering the SIR analysis futile. In Fig. 3.8a 5 users are considered, each uniformly located within each sector $\Delta\theta$ and the resulting SIR, taking 250 realizations, are shown in Fig. 3.8b. The blue curve highlights the average SIR taken from all realizations, while the gray area bounded by the red line highlights the 90% confidence interval (C.I.). From Fig. 3.8b it can be seen that the SIR can vary significantly depending on the exact position of the interferer. This is due to the matching between the pattern of the observable field of the interferer and the antenna pattern. In this case the antenna pattern is taken equal to the observable field pattern of the desired signal.

In Fig. 3.8c a similar scenario with 9 clients is considered. As can be seen from Fig. 3.8d, where the resulting SIR curves are presented, when considering larger structures and thus directive antennas the C.I. of 90% is narrower since $\Delta\theta \approx 13.3^\circ$, which is smaller than $\Delta\theta = 24^\circ$ which was considered in Fig. 3.8b. This restricts the position of the interferers, causing a narrower 90% C.I.. Furthermore, since we are considering more interferers, the antenna size needed to achieve the same SIR is larger. It can be seen that the average SIR is reduced in the case of 9 clients with respect to 5 clients.

3.4 Maximum Number of Beams

This section presents a study on the relation between the SIR when scanning, and the number of links present on the FoV of the antenna. The present study only focuses on the characterization of the SIR in different communication scenarios. However, when considering interference and other forms of noise in the system it is possible to relate the Signal to Noise Ratio (SNR) to the bit error rate (BER), which is the main parameter used to quantify the performance of digital communication systems [32]. As previously mentioned, this study only focuses on the characterization of the interference. Future studies can use the SIR analysis to relate it to a corresponding BER depending on the modulation used, as clarified in [32, Ch. 7], and therefore quantify the maximum number of beams for a desired BER.

In Fig. 3.9 we analyze a square plate of size $r_{\min} = 5\lambda_0$ where we consider a varying number

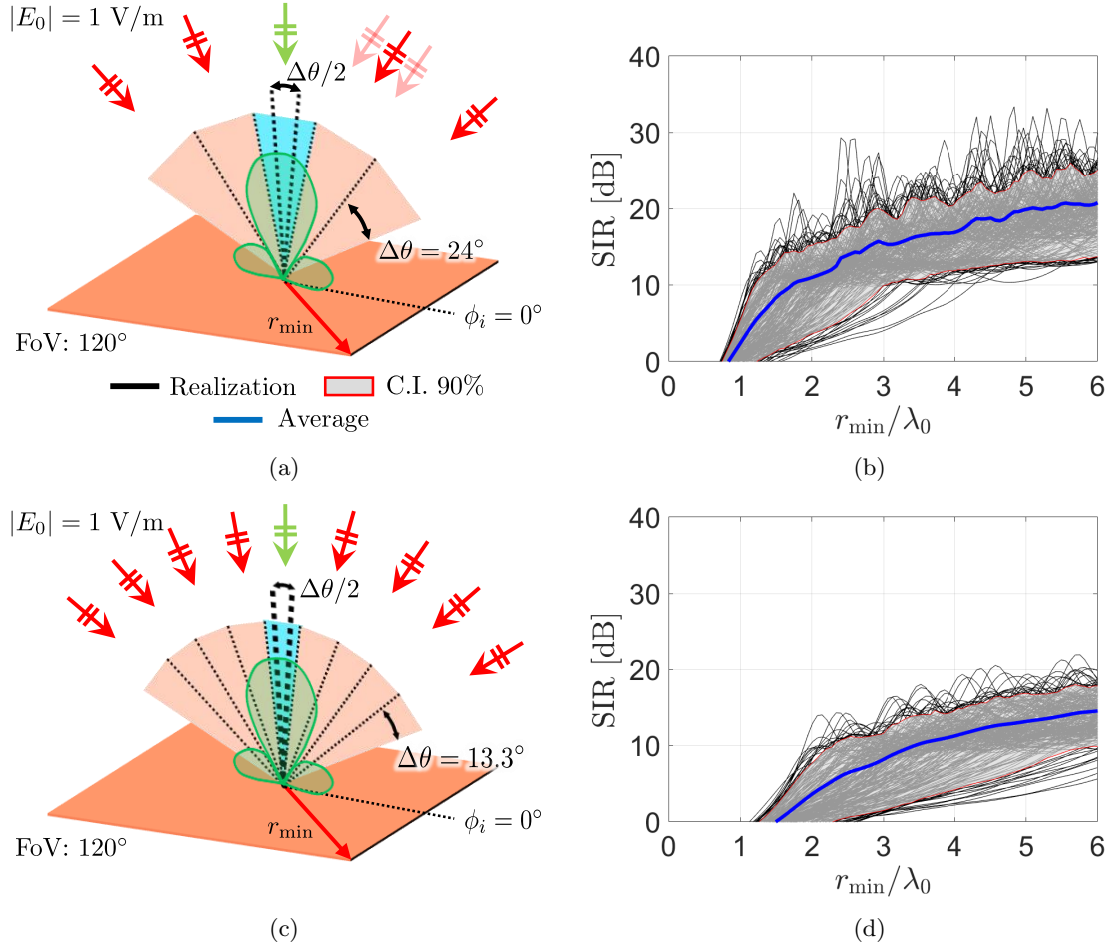


Figure 3.8: (a) Square plate of size r_{\min} with 5 randomly distributed clients, (b) SIR 250 realizations including the average SIR and 90% C.I. considering the signal around broadside and 4 interferers. (c) Square plate of size r_{\min} with 9 randomly distributed clients (d) SIR 250 realizations including the average SIR and 90% C.I. considering the signal around broadside and 8 interferers.

N_l of links, angularly equispaced over a FoV of 120° as shown in Fig. 3.9a. The SIR is shown in Fig. 3.9b as a function of the number of links. The different points for each N_l refer to the SIR when the desired signal is coming from one of the considered directions and all other users are assumed to be interferers. This plot allows estimating the number of links communicating with the antenna for which a certain SIR level can be guaranteed. From Fig. 3.9b we see that depending on the number of links the spread of the variation in SIR can differ. Moreover, it can be noted that the maximum SIR is not necessarily when the desired signal points to broadside, but can differ depending on the number of links. This can be explained by the distribution of the nulls in the antenna pattern with respect to observable field pattern of the interferers. In Fig. 3.10a we consider the case of 7 interferers, angularly equispaced on the FoV. From Fig. 3.9b we can see a large variation in the SIR, which achieves a maximum of 21.6 dB and a minimum of 10.6 dB. The maximum SIR is achieved when the antenna is pointing to the client at broadside and the minimum when pointing to the furthest client located at $\theta_{\text{scan}} = 51.4^\circ$. The difference in SIR can be explained with the aid of Fig. 3.10b, where the antenna pattern in the case of pointing to broadside and the case of pointing to $\theta_{\text{scan}} = 51.4^\circ$ are shown. The vertical dotted lines represent the location of the clients. It can be

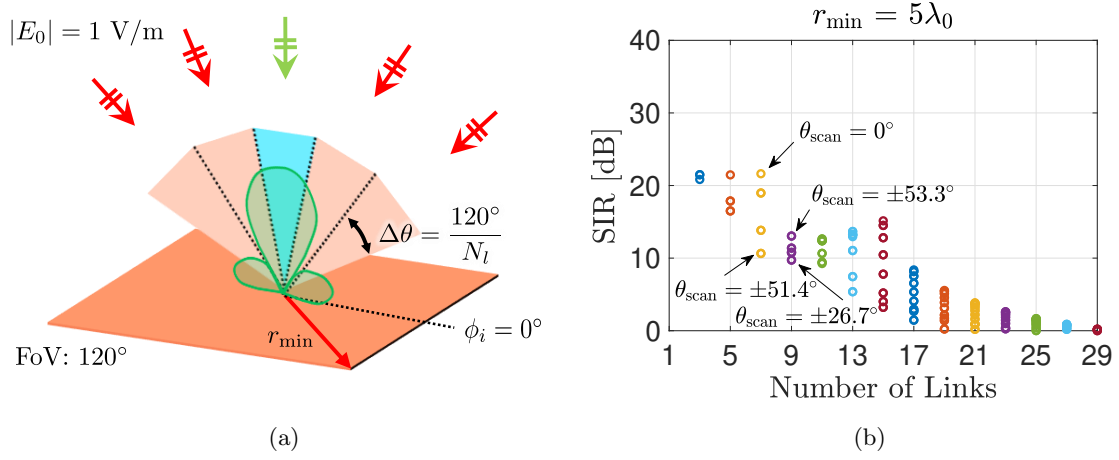


Figure 3.9: (a) Square plate of size $r_{\min} = 5\lambda_0$ with N_l interferers evenly distributed over the FoV. (b) Variation of SIR when scanning to each client for a given number of links.

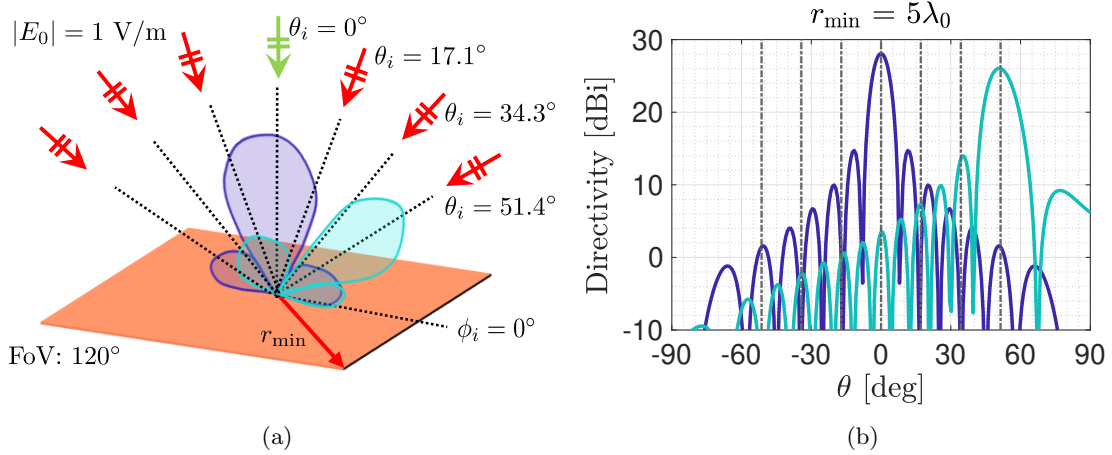


Figure 3.10: (a) Square plate with size $r_{\min} = 5\lambda_0$ with 8 TM plane waves as clients, evenly distributed over a FoV of 120° and (b) antenna patterns for scanning to broadside and $\theta_{\text{scan}} = 51.4^\circ$.

seen from Fig. 3.10b that when pointing to broadside the interferers are conveniently located at the nulls of the pattern. However, in the case of scanning, the interferers are located on the sidelobes of the antenna pattern, thus allowing the antenna to better couple to the interferers and ultimately degrade the SIR.

This Page Intentionally Left Blank

4. SIR Improvement Techniques

The coupling coefficients introduced in Sec. 3.1 can be used to calculate the coupling between the observable field of a certain incident field and the antenna pattern \vec{V}_a^j . By choosing the antenna pattern \vec{V}_a^j to be equal to the one of the observable field \vec{V}_{obs}^j , the coupling coefficient is equal to unity, and the received signal power is maximized. However, this does not ensure the optimum SIR, since it does not necessarily minimize the interference captured. This chapter presents two strategies to improve the SIR, in Sec. 4.1 the effect of applying a taper to the current distribution is investigated and in Sec. 4.2 a null placement technique is investigated.

4.1 Tapered Distribution

A technique used to reduce interference is a tapered aperture distribution. This technique reduces the sidelobe level at the cost of a lower main beam efficiency. The introduction of the taper causes a loss of directivity, broadening the main beam while suppressing the sidelobes. The introduction of a taper in the aperture distribution of the antenna gives rise to a pattern different than the one of the observable field. Therefore, the coupling coefficient has a value lower than one, however, the reduction in sidelobe level reduces the interference captured and thus overall improves the SIR.

The taper is applied to a rectangular domain, and its implementation is analogous to the one described in [33] for circular feeds. In a rectangular domain, the edge tapers along x and y can be applied to the aperture distribution, independently of each other. Let us now consider a Gaussian taper applied along x , but the explanation is analogous for y . The edge taper in linear scale $T_{\text{E,lin}}$ is defined as follows

$$T_{\text{E,lin}} = \frac{E(x_{\text{edge}})}{E(0)} = e^{-\left(\frac{x_{\text{edge}}}{w_x}\right)^2} \quad (4.1)$$

where x_{edge} is $-S_x/2$ and $S_x/2$ as shown in Fig. 4.2a. To synthesize the targeted taper, the weight w_x in (4.1) has to be determined. Since the taper is usually mentioned in decibels, (4.1) can be manipulated as follows

$$e^{-\left(\frac{x_{\text{edge}}}{w_x}\right)^2} = 10^{-\frac{T_{\text{E,dB}}}{20}} \quad (4.2)$$

where $T_{\text{E,dB}}$ is the edge taper expressed in dB. Finally w_x can be calculated as follows

$$w_x = \frac{S_x}{2\sqrt{\frac{T_{\text{E,dB}}}{20} \ln(10)}}. \quad (4.3)$$

Recalling from Sec. 2.4.1 that the field radiated by uniform sources with a linear phase can be calculated as follows

$$\vec{E}(\vec{r}) = jk|E_0| \frac{e^{-jk r}}{4\pi r} \iint_S e^{j\vec{k}_{\text{scan}} \vec{r}'} e^{j\vec{k} \vec{r}'} d\vec{r}' \left[(\underline{\underline{I}} - \hat{r}\hat{r}) \cdot \hat{n} \times (\hat{k}_{\text{scan}} \times \hat{p}_{\text{scan}}) - \hat{r} \times (\hat{n} \times \hat{p}_{\text{scan}}) \right] \quad (4.4)$$

where \hat{k}_{scan} is the desired scan direction and \hat{p}_{scan} is the polarization of the electric field on the aperture. Now by applying an edge taper along x and y the integral in (4.4) becomes as follows

$$\iint_S e^{-\left(\frac{x'}{w_x}\right)^2} e^{-\left(\frac{y'}{w_y}\right)^2} e^{j\vec{k}_{\text{scan}} \vec{r}'} e^{j\vec{k} \vec{r}'} d\vec{r}'. \quad (4.5)$$

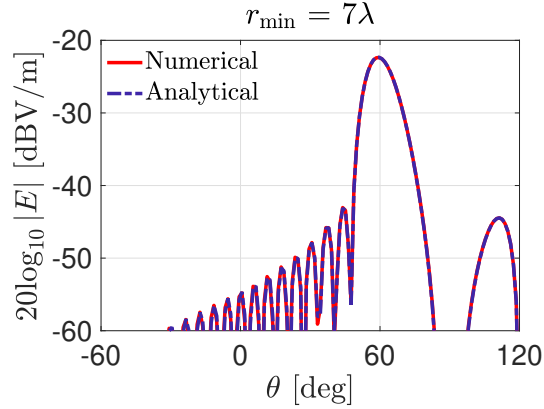


Figure 4.1: Validation of analytical implementation of the pattern radiated by a 10 dB tapered aperture distribution along x and y for the case of scanning at 60° .

By splitting the double integral into the x' and y' variables we can write

$$\iint_S e^{-\left(\frac{x'}{w_x}\right)^2} e^{-\left(\frac{y'}{w_y}\right)^2} e^{j\vec{k}_{\text{scan}}\vec{r}'} e^{j\vec{k}\vec{r}'} d\vec{r}' = \int_{-S_x/2}^{S_x/2} e^{-\left(\frac{x'}{w_x}\right)^2} e^{j(k_{\text{scan},x}+k_x)x'} dx' \int_{-S_y/2}^{S_y/2} e^{-\left(\frac{y'}{w_y}\right)^2} e^{j(k_{\text{scan},y}+k_y)y'} dy'. \quad (4.6)$$

The solution of these integrals has been derived in Appendix D and takes the following form

$$\int_{-S_x/2}^{S_x/2} e^{-\left(\frac{x'}{w_x}\right)^2} e^{j(k_{\text{scan},x}+k_x)x'} dx' = \frac{w_x}{2} \sqrt{\pi} e^{-\frac{w_x^2(k_{\text{scan},x}+k_x)^2}{4}} \left[\text{erf}\left(\frac{j(k_{\text{scan},x}+k_x)w_x^2+S_x}{2w_x}\right) - \text{erf}\left(\frac{j(k_{\text{scan},x}+k_x)w_x^2-S_x}{2w_x}\right) \right] \quad (4.7)$$

where the error function $\text{erf}(x)$ is used. A similar solution holds for the case of the integral in y' . This solution is compared with the results acquired from numerical integration and are shown in Fig. 4.1.

In Fig. 4.2, the directivity patterns of a 10 dB Gaussian taper are compared with a uniform distribution, i.e., the one radiating the observable field, for three different structure sizes as in Fig. 4.2a. In Fig. 4.2b where a structure of size $r_{\text{min}} = 0.5\lambda_0$ is considered it can be seen that the taper has minimal effect for small structures. In Fig. 4.2c and more clearly in Fig. 4.2d, where structures of size $r_{\text{min}} = \lambda_0$ and $r_{\text{min}} = 7\lambda_0$ are considered, respectively, the effect of tapering can be seen on the sidelobe level. However, in both cases it can be seen that the sidelobe suppression comes at the cost of a broader main beam and reduced directivity. In Fig. 4.3 the SIR is assessed for the use of such a taper, where 10 dB Gaussian tapering is used along both dimension of the square structure. The structure considered is the one in Fig. 4.3a where r_{min} is the radius of the minimum enveloping sphere and the structure is under illumination of three TM plane waves impinging from $\theta_i = 0^\circ$, $\theta_i = 30^\circ$ and $\theta_i = 60^\circ$. The resulting SIR versus the size in terms of the wavelength is shown in Fig. 4.3b, when the antenna is scanning to $\theta_{\text{scan}} = 0^\circ$ and $\theta_{\text{scan}} = 60^\circ$. The frequency of simulation is of 100 GHz. From Fig. 4.3b it can be seen that in the case of small structures as expected the use of a taper does not provide an improvement in the SIR due to the loss of directivity.

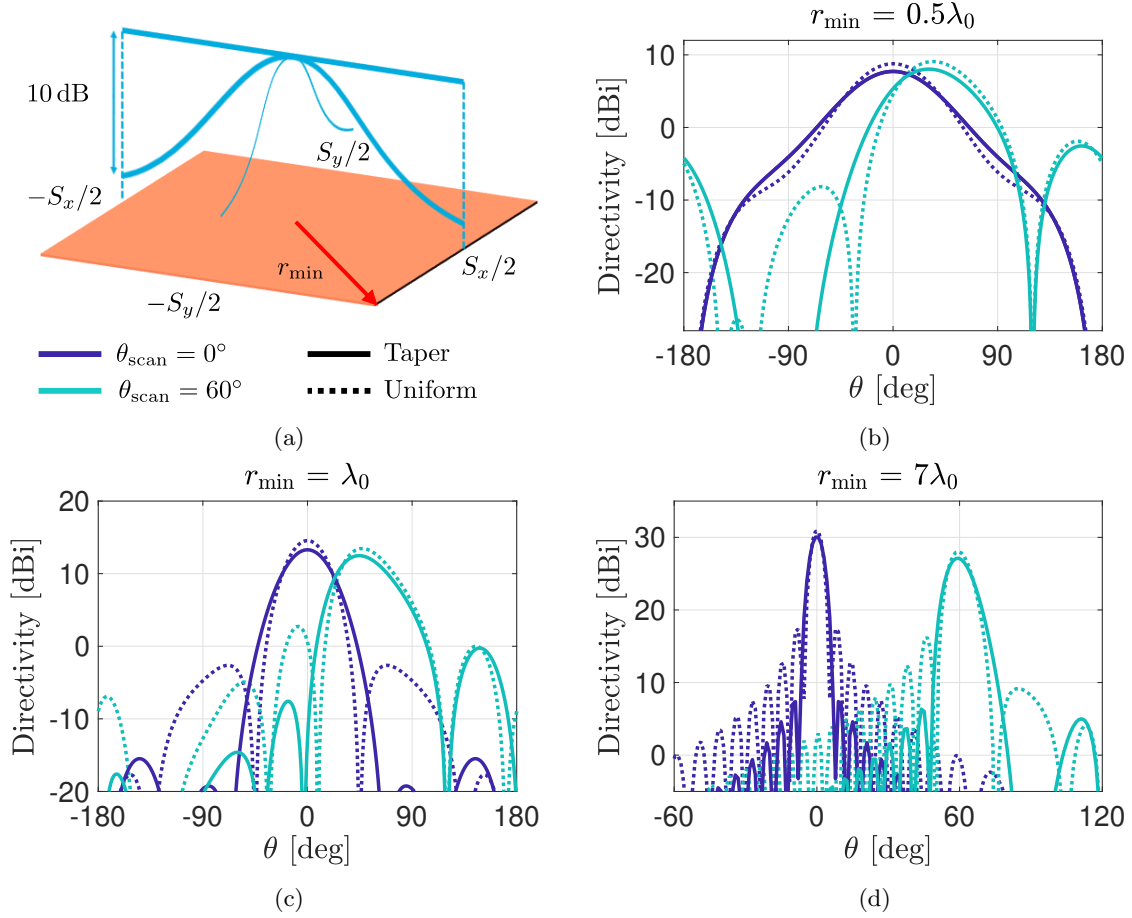


Figure 4.2: Comparison of directivity patterns between (a) a square plate for a 10 dB Gaussian taper and a uniform distribution in the case of (b) $r_{\min} = 0.5\lambda_0$, (c) $r_{\min} = \lambda_0$ and (d) $r_{\min} = 7\lambda_0$.

However, in the case of larger structures, starting from $r_{\min} \approx 2\lambda_0$, the reduction in sidelobe level provides an overall better SIR.

4.2 Nulling

The capability of placing a null for a specific direction in an antenna pattern can help reduce the interference in a given communication scenario. The method consists of using a correction pattern in superposition with the original antenna pattern resulting from the observable field to place a null in the direction of an interferer. In order to assess the SIR improvement from this technique we first present a case where no nulling is used. As depicted in Fig. 4.4a, a square plate enveloped by a minimum sphere of radius r_{\min} is considered, with two clients at $\theta_i = 0^\circ$ and $\theta_i = 40^\circ$, where the signal is the client at broadside. The SIR versus the size of the structure for such a configuration can be seen in Fig. 4.4b. As can be seen from Fig. 4.4b, the SIR achieves its local maxima when the size of the structure is characterized by $r_{\min} \approx 1.16\lambda_0$ this can be explained with the aid of Fig. 4.5a, where the antenna pattern and the pattern of the observable field of the interferer, located at $\theta_i = 40^\circ$, are shown. From Fig. 4.5a, it can be seen that for this specific antenna size, the antenna pattern naturally has a null at the maximum of the observable field pattern of the interferer. Since

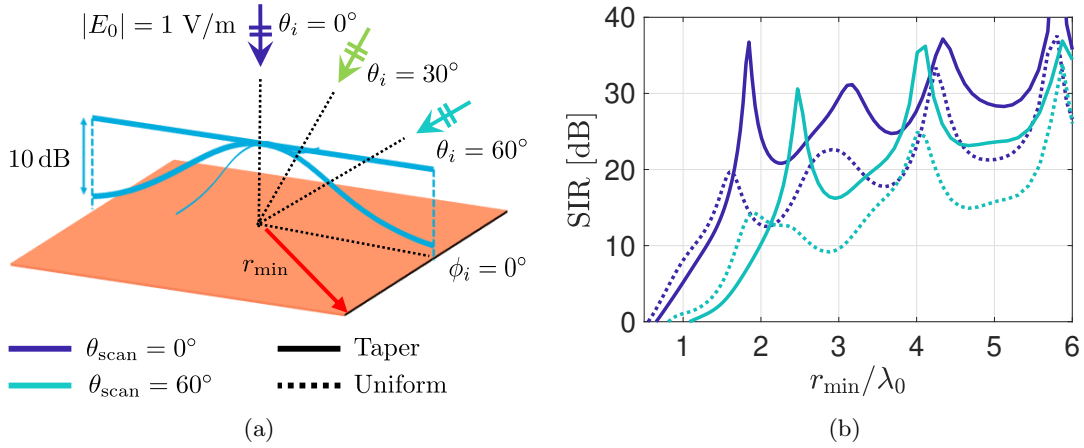


Figure 4.3: SIR analysis in the presence of three TM plane waves impinging from $\theta_i = 0^\circ$, $\theta_i = 30^\circ$ and $\theta_i = 60^\circ$ for a (a) square plate antenna enveloped by a sphere having minimum radius r_{\min} and (b) the resulting SIR when the antenna is pointing to broadside and scanning at 60° for a uniform and 10 dB Gaussian taper.

the power received depends on the coupling between the patterns, as clarified by the use of the coupling coefficient as in (3.8), the null of the antenna pattern located at the maximum of the observable field's pattern of the interferer greatly reduces the power received from the interferer, therefore improving the SIR. Furthermore, for medium-sized antennas, it can be seen from Fig. 4.4b that the local minimum happens for $r_{\min} \approx 1.64\lambda_0$, which can be explained by Fig. 4.5b where it can be seen that for this antenna size, the antenna pattern has its first sidelobe coinciding with the maximum of the observable field's pattern of the interferer, therefore providing a better coupling to the interference and thus degrading the SIR.

To improve the SIR, a simple null placement strategy is presented. In this case, we consider the same scenario as presented in Fig. 4.4a, where the signal is located at broadside, and a single interferer is considered, located at $\theta_i = 40^\circ$. In Fig. 4.6a the antenna pattern can be seen in the case where it is taken to be the pattern of the observable field of the signal. To place a null, we first synthesize a pattern that points to the desired null location as in Fig. 4.6b. This pattern is then weighted by the value of the original pattern at the desired null location as shown in Fig. 4.6c. By subtracting the two patterns, the targeted pattern with a null at the desired location can be obtained, as shown in Fig. 4.6d.

Now we consider the same situation with the signal at $\theta_i = 0^\circ$ and the interferer at $\theta_i = 40^\circ$ as shown in Fig. 4.7a for which we apply the null placement strategy for every antenna size in order to improve the SIR, the results are shown in Fig. 4.7b. It can be seen that the SIR is improved overall, except at the local maxima, this can be explained by other nulls that occur in the original pattern which further reduces the interference at this specific antenna size.

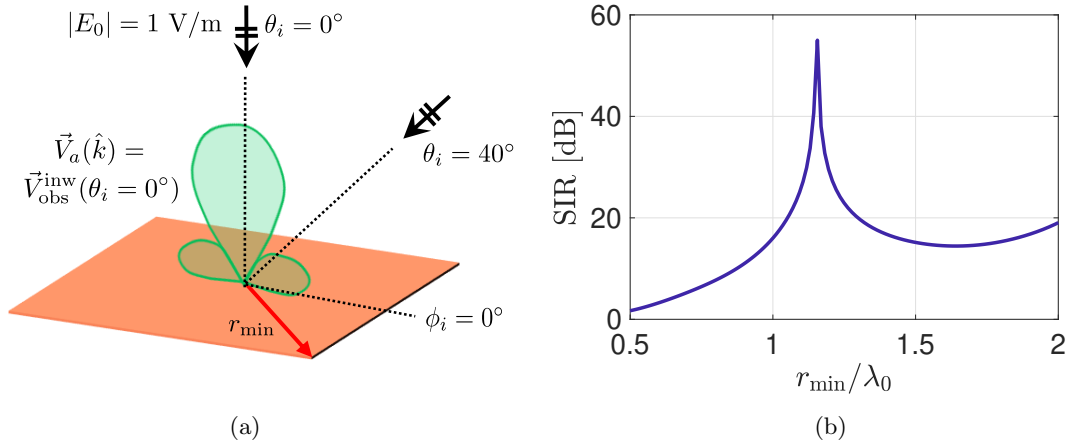


Figure 4.4: SIR analysis for a (a) square plate with minimum enveloping sphere of radius r_{\min} with two clients at $\theta_i = 0^\circ$ and $\theta_i = 40^\circ$ with the antenna pointing to broadside. In (b) the resulting SIR.

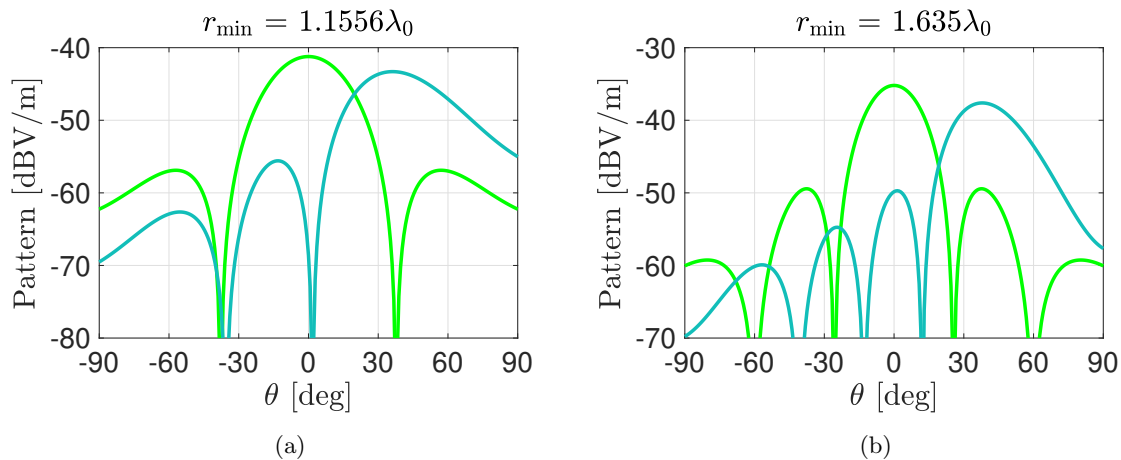


Figure 4.5: Antenna pattern and pattern of the observable field of the interferer located at $\theta_i = 40^\circ$ in the case of (a) a structure with size when the maximum SIR occurs and (b) when the minimum SIR occurs.

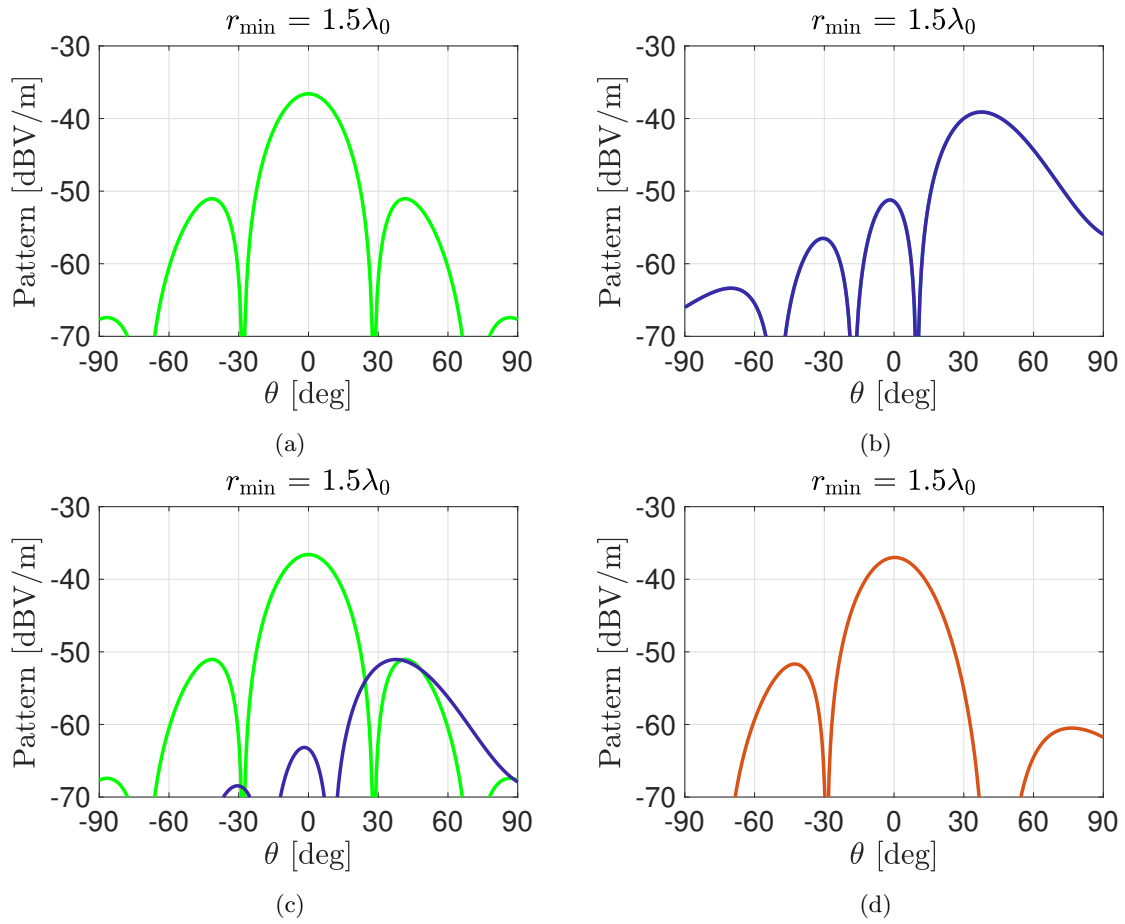


Figure 4.6: Antenna patterns for (a) pointing to broadside without null placement, (b) scanning to the desired null position, (c) original pattern and weighted scanning pattern and (d) final pattern with null placed at desired angle.

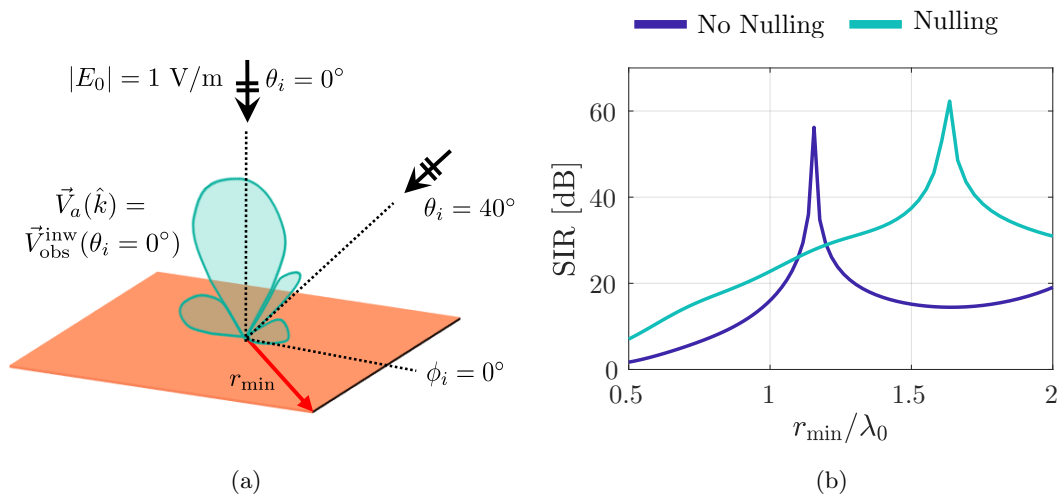


Figure 4.7: SIR analysis for (a) a structure using nulling at the interferers angle. In (b) resulting SIR using the null placement strategy compared to the case of a uniform distribution.

This Page Intentionally Left Blank

5. Conclusions and Future Work

5.1 Summary and Conclusions

In this thesis a fundamental study on the number of independent beams that can be supported by radiating apertures characterized by planar domains was presented. Antennas with rectangular and circular domains were considered. This study is relevant to determine, in a multi-beam communication scenario, the maximum number of links supported by the antenna, for a given size and geometry. The independence between beams, and in turn the number of supported links, was quantified in terms of the SIR.

In order to calculate the SIR, the concept of the observable field was presented. The observable field allows us to calculate the maximum power available to structures contained in a finite volume. It was shown that using the PO currents to calculate the observable field renders the power available continuous with the size of the structure. A comparison was made with older methods resorting to the spherical modes. Unlike the method proposed here, spherical mode expansion results in discrete values of the estimated power available, because of the integer number of modes that are considered.

The PO currents were used to derive the formulas for the patterns of the observable field for planar structures. The derivation of the closed-form Fourier transform of the current distributions allowed for a faster implementation when calculating the power associated with the fields. The results obtained with planar rectangular and circular distributions were compared with results for the case of spherical domains. The directivity patterns of the rectangular and circular structure showed a scan loss, which does not occur for spherical structures. The estimation of scan loss is relevant for realistic base station antennas, that are typically implemented as planar phased arrays.

Once the framework of the observable field theory was established, an analysis on the interference between different beams was presented. Coupling coefficients were introduced, defined as the coupling between an antenna pattern and the pattern of the observable field. These coefficients are convenient because they can be used to evaluate both the power associated with the desired signal and the interference. The coupling coefficient also allows to define the efficiency of antennas of arbitrary size. The efficiency is 1 if the antenna receives the entire observable power and less than 1 otherwise. This definition is a more suitable figure of merit for antenna performance, as compared with the aperture efficiency, which is known to exceed 1 for electrically small antennas.

Calculating the power received by an antenna communicating with multiple clients requires the calculation of multiple double integrals, i.e., the coupling between the antenna pattern and the observable field of each client and the power associated with the observable field of each client. This poses a numerically intensive task, to this aid the Gauss - Legendre quadrature was used in combination with a uniform quadrature to accelerate the calculation of the integrals.

Using the coupling coefficients the SIR in the case of multiple plane waves was calculated for a square plate, a disk and compared with the sphere. It was seen that the disk and the sphere achieve similar SIRs, the disk performing slightly better due to the scan loss limiting the contribution of the interferers. Furthermore, the SIR achieved by the square plate is lower when comparing the same structure size in terms of the radius of minimum enveloping sphere. This is due to the smaller aperture area associated with the square plate with respect to the disk when considering the same minimum enveloping sphere.

The SIR was analyzed in different scenarios, considering scanning to different clients and randomly located interferers. Furthermore, the number of links possible for a given SIR was presented.

Finally, two techniques were researched to improve the SIR. To reduce the contribution of the interferers a Gaussian taper can be applied on the aperture distribution. This decreases the signal received slightly, but due to the reduction in sidelobe level, the reduced interference captured overall, improves the SIR for a certain antenna dimension. Furthermore, in order to reduce the interference from a given direction an antenna pattern can be synthesized with a null placed at such direction.

5.2 Future Work

The work described in this thesis opens the possibility of future developments and research activities:

- A Graphical User Interface (GUI) is being developed in order to ease the analysis of different antenna geometries in certain communication scenario, allowing for a systematic comparison between different cases.
- The results shown in the thesis referred to ideal continuous current distributions. The application of the findings to real antenna arrays was not addressed. However, wideband antenna arrays with different size have been designed and manufactured in the group. Thus, these prototypes can be used to experimentally validate the results presented in this thesis.
- A study on the optimization of the SIR over large bandwidths is also of interest. The present work considers antennas with a certain size at a specific frequency. On the contrary, the above mentioned wideband antenna arrays have varying electrical size within the large band of operation.
- Relating the observable power to the different beamforming architectures is also an interesting topic for future investigation. Base station phased array can use analog, digital or hybrid beamformers. The different choices of the beamforming strategy could be compared in terms of observable power.

A. Observable Field for Generalized Incidence

The procedure presented in Sec. 2.3 can also be generalized for non plane wave incidences. In this case the incident field, in the absence of the antenna, can be decomposed into a superposition of homogeneous plane waves in the following way

$$\vec{E}_{\text{inc}}(\vec{r}) = \iint_S \vec{E}_{\text{inc}}^{\text{PWS}}(\hat{k}_{\text{inc}}) e^{-j\vec{k}_{\text{inc}} \cdot \vec{r}} d\hat{k}_{\text{inc}} \quad (\text{A.1})$$

where \vec{r} is the observation point on the antenna domain. Furthermore, $\vec{E}_{\text{inc}}^{\text{PWS}}$ is the Plane Wave Spectrum (PWS) associated with the incident field. The magnetic field can then be calculated as

$$\vec{H}_{\text{inc}}^{\text{PWS}} = \frac{1}{\zeta} \hat{k}_{\text{inc}} \times \vec{E}_{\text{inc}}^{\text{PWS}}. \quad (\text{A.2})$$

In this case, for each component of the PWS in (A.1), the set of equivalent currents resulting from the PO can be calculated as

$$\vec{J}_{\text{PO},i}^{\text{out}}(\hat{k}_{\text{inc}}, \vec{r}) = \begin{cases} -\hat{n} \times \vec{H}_{\text{inc}}^{\text{PWS}}(\hat{k}_{\text{inc}}) e^{-j\vec{k}_{\text{inc}} \cdot \vec{r}}, & \text{if } \hat{n} \cdot \hat{k}_{\text{inc}} < 0 \\ 0 & \text{otherwise} \end{cases} \quad (\text{A.3})$$

$$\vec{M}_{\text{PO},i}^{\text{out}}(\hat{k}_{\text{inc}}, \vec{r}) = \begin{cases} \hat{n} \times \vec{E}_{\text{inc}}^{\text{PWS}}(\hat{k}_{\text{inc}}) e^{-j\vec{k}_{\text{inc}} \cdot \vec{r}}, & \text{if } \hat{n} \cdot \hat{k}_{\text{inc}} < 0 \\ 0 & \text{otherwise.} \end{cases} \quad (\text{A.4})$$

The observable field can then be calculated as the field radiated by the superposition of all these current distributions as follows

$$\vec{J}_{\text{PO,tot}}^{\text{out}}(\vec{r}) = \iint_S \vec{J}_{\text{PO},i}^{\text{out}}(\hat{k}_{\text{inc}}, \vec{r}) d\hat{k}_{\text{inc}} \quad (\text{A.5})$$

$$\vec{M}_{\text{PO,tot}}^{\text{out}}(\vec{r}) = \iint_S \vec{M}_{\text{PO},i}^{\text{out}}(\hat{k}_{\text{inc}}, \vec{r}) d\hat{k}_{\text{inc}}. \quad (\text{A.6})$$

As an example consider two TM polarized plane waves impinging from $\theta_i = 30^\circ$ and $\theta_i = -30^\circ$ on a square plate characterized by the size $r_{\text{min}} = 2\sqrt{2}\lambda_0$ as depicted in Fig. A.1. The time domain PO currents, both electric and magnetic, are presented in Fig. A.2a and Fig. A.2b, respectively. Using these currents the observable field pattern can be calculated, this is shown in Fig. A.3.

A.1 The Generalized Amplification Factor

In Subsec. 2.3.1 the amplification factor α , for the case of plane wave incidence was presented. However, when dealing with a generalized incidence the procedure presented in Subsec. 2.3.1 is no longer valid.

Consider a generalized incident field \vec{f}_{inc} , which can be related to the field radiated by the PO currents, the amplification factor α and the remaining field as follows

$$\vec{f}_{\text{inc}} = \alpha \vec{f}_{\text{PO}} + \vec{f}_{\text{rem}}. \quad (\text{A.7})$$

In order to calculate α we can resort to the field reaction integral. The reaction integral between the incident field $\vec{f}_{\text{inc}} = \begin{bmatrix} \vec{E}_{\text{inc}} \\ \vec{H}_{\text{inc}} \end{bmatrix}$ and a testing field $\vec{f}_t = \begin{bmatrix} \vec{E}_t \\ \vec{H}_t \end{bmatrix}$, is defined as follows

$$\langle \vec{f}_{\text{inc}}, \vec{f}_t \rangle \equiv \iint_{S_\infty} \left[\frac{1}{\zeta} \vec{E}_{\text{inc}} \cdot \vec{E}_t - \zeta \vec{H}_{\text{inc}} \cdot \vec{H}_t \right] d\vec{r}_\infty \quad (\text{A.8})$$

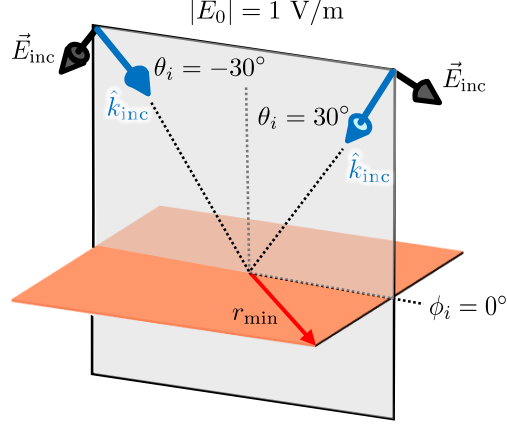


Figure A.1: Square plate of size $r_{\min} = 2\sqrt{2}\lambda_0$ illuminated by two TM polarized plane waves impinging from $\theta_i = \pm 30^\circ$.

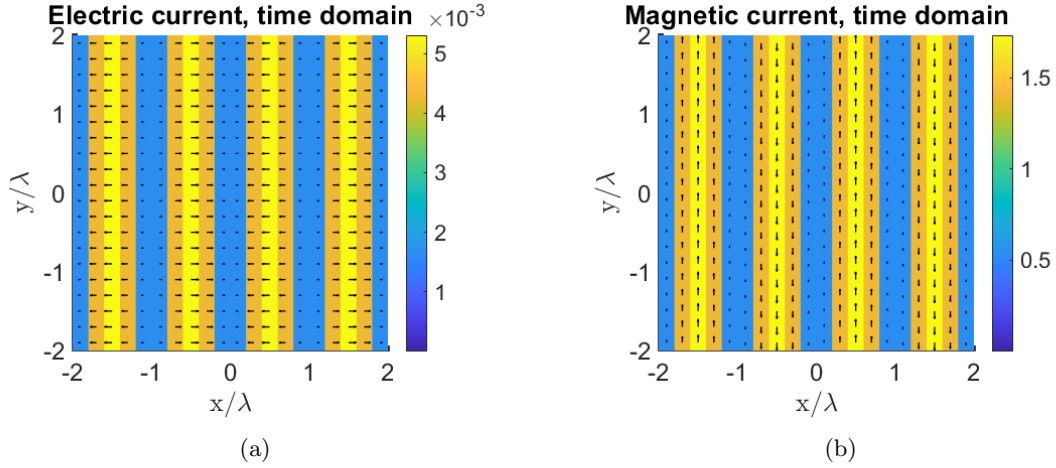


Figure A.2: (a) Electric and (b) magnetic PO currents in the time domain.

where the integral is evaluated in the far field of the antenna, \vec{E} represents the electric field and \vec{H} represents the magnetic field. By multiplying (A.7) with a testing field we can write (A.7) as follows

$$\langle \vec{f}_{\text{inc}}, \vec{f}_t \rangle = \alpha \langle \vec{f}_{\text{PO}}, \vec{f}_t \rangle + \langle \vec{f}_{\text{rem}}, \vec{f}_t \rangle. \quad (\text{A.9})$$

A convenient choice of a testing field is the one radiated by the antenna with equal pattern to the inward observable field. This field \vec{f}_{tx} , radiated by the antenna when operated in transmission, has the following properties

$$\vec{E}_{\text{tx}}(\vec{r}) = \vec{V}_{\text{PO}}^{\text{inw}*}(\hat{k}) \frac{e^{-jkr}}{r} \quad (\text{A.10a})$$

$$\vec{H}_{\text{tx}}(\vec{r}) = \frac{1}{\zeta} \hat{k} \times \vec{E}_{\text{tx}}(\vec{r}). \quad (\text{A.10b})$$

Since the field \vec{f}_{tx} has the same pattern as the inward observable field, the reaction integral between the remaining field and \vec{f}_{tx} can be approximated as $\langle \vec{f}_{\text{rem}}, \vec{f}_{\text{tx}} \rangle \approx 0$. Therefore, (A.9) can be rewritten

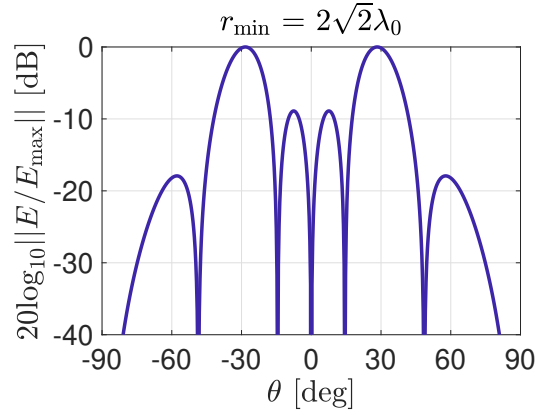


Figure A.3: Far-field pattern of the observable field in the case of two TM plane waves impinging from $\theta_i = \pm 30^\circ$.

to calculate α as follows

$$\alpha \approx \frac{\langle \vec{f}_{\text{inc}}, \vec{f}_{\text{tx}} \rangle}{\langle \vec{f}_{\text{PO}}, \vec{f}_{\text{tx}} \rangle}. \quad (\text{A.11})$$

As described in [18] the denominator in (A.11) can be demonstrated to be $\langle \vec{f}_{\text{PO}}, \vec{f}_{\text{tx}} \rangle = 4P_{\text{PO}}$, where P_{PO} is the power radiated by the PO currents.

This Page Intentionally Left Blank

B. Radiation from a Rectangular Aperture

This appendix presents the derivation of the electric and magnetic far field radiated by a uniform current distribution with linear phase on a rectangular aperture. This is the case when calculating the observable field from a plane wave impinging on a rectangular antenna structure from a particular incidence angle.

First, we consider a plane wave described by its electric field with polarization \hat{p}_{inc} and magnitude $|E_0|$ as

$$\vec{E}_{\text{inc}} = |E_0| e^{-j\vec{k}_{\text{inc}}\vec{r}'} \hat{p}_{\text{inc}} \quad (\text{B.1})$$

and its magnetic field as

$$\vec{H}_{\text{inc}} = \frac{1}{\zeta} \hat{k}_{\text{inc}} \times \vec{E}_{\text{inc}}. \quad (\text{B.2})$$

where \vec{k}_{inc} is the propagation vector of the incident field, which can be written as

$$\vec{k}_{\text{inc}} = \begin{bmatrix} k_{\text{inc},x} \\ k_{\text{inc},y} \\ k_{\text{inc},z} \end{bmatrix} = -k_0 \begin{bmatrix} \sin \theta_i \cos \phi_i \\ \sin \theta_i \sin \phi_i \\ \cos \theta_i \end{bmatrix} \quad (\text{B.3})$$

with θ_i and ϕ_i the angles of incidence.

Using the PO currents method explained in Section 2.3, the currents that give rise to a field with the same pattern as the inward observable field have the following distribution on the rectangular surface

$$\vec{J}_{\text{obs}}^{\text{inw}} = \alpha \frac{1}{\zeta} |E_0| e^{j\vec{k}_{\text{inc}}\vec{r}'} \hat{n} \times (\hat{k}_{\text{inc}} \times \hat{p}_{\text{inc}}) \quad (\text{B.4a})$$

$$\vec{M}_{\text{obs}}^{\text{inw}} = \alpha |E_0| e^{j\vec{k}_{\text{inc}}\vec{r}'} \hat{n} \times \hat{p}_{\text{inc}}. \quad (\text{B.4b})$$

Where the transformations explained in (2.27a) and (2.27b) have been taken into account.

Recalling the radiation integral in (2.39) for the electric far field and substituting (B.4a) and (B.4b) we can write (2.39) as follows

$$\begin{aligned} \vec{E}(\vec{r}) = & -j\omega\mu \frac{e^{-jk r}}{4\pi r} (\underline{\underline{I}} - \hat{r}\hat{r}) \cdot \iint_S \alpha \frac{1}{\zeta} |E_0| e^{j\vec{k}_{\text{inc}}\vec{r}'} \hat{n} \times (\hat{k}_{\text{inc}} \times \hat{p}_{\text{inc}}) e^{j\vec{k}\vec{r}'} d\vec{r}' \\ & + jk \frac{e^{-jk r}}{4\pi r} \hat{r} \times \iint_S \alpha |E_0| e^{j\vec{k}_{\text{inc}}\vec{r}'} (\hat{n} \times \hat{p}_{\text{inc}}) e^{j\vec{k}\vec{r}'} d\vec{r}'. \end{aligned} \quad (\text{B.5})$$

By rearranging the terms in (B.5) it can be rewritten as

$$\begin{aligned} \vec{E}(\vec{r}) = & -j\omega\mu \frac{1}{\zeta} \alpha |E_0| \frac{e^{-jk r}}{4\pi r} (\underline{\underline{I}} - \hat{r}\hat{r}) \cdot \hat{n} \times (\hat{k}_{\text{inc}} \times \hat{p}_{\text{inc}}) \iint_S e^{j\vec{k}_{\text{inc}}\vec{r}'} e^{j\vec{k}\vec{r}'} d\vec{r}' \\ & + jk\alpha |E_0| \frac{e^{-jk r}}{4\pi r} \hat{r} \times (\hat{n} \times \hat{p}_{\text{inc}}) \iint_S e^{j\vec{k}_{\text{inc}}\vec{r}'} e^{j\vec{k}\vec{r}'} d\vec{r}'. \end{aligned} \quad (\text{B.6})$$

Recognizing that $\omega\mu \frac{1}{\zeta} = k$ we can rewrite (B.6) as follows

$$\vec{E}(\vec{r}) = -jk\alpha |E_0| \frac{e^{-jk r}}{4\pi r} \iint_S e^{j\vec{k}_{\text{inc}}\vec{r}'} e^{j\vec{k}\vec{r}'} d\vec{r}' \left[(\underline{\underline{I}} - \hat{r}\hat{r}) \cdot \hat{n} \times (\hat{k}_{\text{inc}} \times \hat{p}_{\text{inc}}) - \hat{r} \times (\hat{n} \times \hat{p}_{\text{inc}}) \right]. \quad (\text{B.7})$$

In order to solve the integral, the observation propagation vector \vec{k} can be written in its cartesian components as

$$\vec{k} = \begin{bmatrix} k_x \\ k_y \\ k_z \end{bmatrix} = k_0 \begin{bmatrix} \sin \theta \cos \phi \\ \sin \theta \sin \phi \\ \cos \theta \end{bmatrix}. \quad (\text{B.8})$$

Furthermore, the domain of integration can be represented by the vector \vec{r}' as follows

$$\vec{r}' = \begin{bmatrix} x' \\ y' \\ 0 \end{bmatrix}. \quad (\text{B.9})$$

Moreover, considering that the antenna structure has size S_x along the x direction and S_y along the y direction, the integral in (B.7) can be rewritten as

$$\begin{aligned} \iint_S e^{j\vec{k}_{\text{inc}}\vec{r}'} e^{j\vec{k}\vec{r}'} d\vec{r}' &= \int_{-S_x/2}^{S_x/2} \int_{-S_y/2}^{S_y/2} e^{j(k_{\text{inc},x}x' + k_{\text{inc},y}y')} e^{j(k_x x' + k_y y')} dx' dy' \\ &= \int_{-S_x/2}^{S_x/2} \int_{-S_y/2}^{S_y/2} e^{j(k_{\text{inc},x} + k_x)x'} e^{j(k_{\text{inc},y} + k_y)y'} dx' dy' \\ &= \int_{-S_x/2}^{S_x/2} e^{j(k_{\text{inc},x} + k_x)x'} dx' \int_{-S_y/2}^{S_y/2} e^{j(k_{\text{inc},y} + k_y)y'} dy'. \end{aligned} \quad (\text{B.10})$$

For which the solution is known and can be written as follows

$$\iint_S e^{j\vec{k}_{\text{inc}}\vec{r}'} e^{j\vec{k}\vec{r}'} d\vec{r}' = S_x \text{sinc}\left(\frac{S_x(k_{\text{inc},x} + k_x)}{2}\right) S_y \text{sinc}\left(\frac{S_y(k_{\text{inc},y} + k_y)}{2}\right). \quad (\text{B.11})$$

It is important to realize that $S_x S_y = A_{\text{ph}}$ is the physical area of the structure. Hence, the electric far field radiated by uniform current with linear phase can be written as

$$\begin{aligned} \vec{E}(\vec{r}) &= -jk\alpha |E_0| \frac{e^{-jkr}}{4\pi r} A_{\text{ph}} \text{sinc}\left(\frac{S_x(k_{\text{inc},x} + k_{\text{obs},x})}{2}\right) \\ &\quad \text{sinc}\left(\frac{S_y(k_{\text{inc},y} + k_{\text{obs},y})}{2}\right) \left[(\underline{I} - \hat{r}\hat{r}) \cdot \hat{n} \times (\hat{k}_{\text{inc}} \times \hat{p}_{\text{inc}}) - \hat{r} \times (\hat{n} \times \hat{p}_{\text{inc}}) \right]. \end{aligned} \quad (\text{B.12})$$

C. Radiation from a Circular Aperture

This appendix presents the derivation of the electric and magnetic far field radiated by a uniform current distribution with linear phase on a circular aperture. This is the case when calculating the observable field from a plane wave impinging on a planar circular antenna structure from a particular incidence angle.

First, we consider a plane wave described by its electric field with polarization \hat{p}_{inc} and magnitude $|E_0|$ as

$$\vec{E}_{\text{inc}} = |E_0| e^{-j\vec{k}_{\text{inc}}\vec{r}'} \hat{p}_{\text{inc}} \quad (\text{C.1})$$

and its magnetic field as

$$\vec{H}_{\text{inc}} = \frac{1}{\zeta} \hat{k}_{\text{inc}} \times \vec{E}_{\text{inc}}. \quad (\text{C.2})$$

where \vec{k}_{inc} is the propagation vector of the incident field, which can be written as

$$\vec{k}_{\text{inc}} = \begin{bmatrix} k_{\text{inc},x} \\ k_{\text{inc},y} \\ k_{\text{inc},z} \end{bmatrix} = -k_0 \begin{bmatrix} \sin \theta_i \cos \phi_i \\ \sin \theta_i \sin \phi_i \\ \cos \theta_i \end{bmatrix} \quad (\text{C.3})$$

with θ_i and ϕ_i the angles of incidence.

Using the PO currents method explained in Section 2.3, the currents that give rise to a field with the same pattern as the inward observable field have the following distribution on the circular surface

$$\vec{J}_{\text{obs}}^{\text{inw}} = \alpha \frac{1}{\zeta} |E_0| e^{j\vec{k}_{\text{inc}}\vec{r}'} \hat{n} \times (\hat{k}_{\text{inc}} \times \hat{p}_{\text{inc}}) \quad (\text{C.4a})$$

$$\vec{M}_{\text{obs}}^{\text{inw}} = \alpha |E_0| e^{j\vec{k}_{\text{inc}}\vec{r}'} \hat{n} \times \hat{p}_{\text{inc}} \quad (\text{C.4b})$$

where the transformations explained in (2.27a) and (2.27b) have been taken into account.

Recalling the radiation integral in (2.39) for the electric far field and substituting (C.4a) and (C.4b) we can write (2.39) as follows

$$\begin{aligned} \vec{E}(\vec{r}) = & -j\omega\mu \frac{e^{-jk r}}{4\pi r} (\underline{\underline{I}} - \hat{r}\hat{r}) \cdot \iint_D \alpha \frac{1}{\zeta} |E_0| e^{j\vec{k}_{\text{inc}}\vec{r}'} \hat{n} \times (\hat{k}_{\text{inc}} \times \hat{p}_{\text{inc}}) e^{j\vec{k}\vec{r}'} d\vec{r}' \\ & + jk \frac{e^{-jk r}}{4\pi r} \hat{r} \times \iint_D \alpha |E_0| e^{j\vec{k}_{\text{inc}}\vec{r}'} (\hat{n} \times \hat{p}_{\text{inc}}) e^{j\vec{k}\vec{r}'} d\vec{r}' \end{aligned} \quad (\text{C.5})$$

where D is a disk, with radius a , representing the aperture in question. By rearranging the terms in (C.5) it can be rewritten as

$$\begin{aligned} \vec{E}(\vec{r}) = & -j\omega\mu \frac{1}{\zeta} \alpha |E_0| \frac{e^{-jk r}}{4\pi r} (\underline{\underline{I}} - \hat{r}\hat{r}) \cdot \hat{n} \times (\hat{k}_{\text{inc}} \times \hat{p}_{\text{inc}}) \iint_D e^{j\vec{k}_{\text{inc}}\vec{r}'} e^{j\vec{k}\vec{r}'} d\vec{r}' \\ & + jk\alpha |E_0| \frac{e^{-jk r}}{4\pi r} \hat{r} \times (\hat{n} \times \hat{p}_{\text{inc}}) \iint_D e^{j\vec{k}_{\text{inc}}\vec{r}'} e^{j\vec{k}\vec{r}'} d\vec{r}'. \end{aligned} \quad (\text{C.6})$$

Recognizing that $\omega\mu \frac{1}{\zeta} = k$ we can rewrite (C.6) as follows

$$\vec{E}(\vec{r}) = -jk\alpha |E_0| \frac{e^{-jk r}}{4\pi r} \iint_D e^{j\vec{k}_{\text{inc}}\vec{r}'} e^{j\vec{k}\vec{r}'} d\vec{r}' \left[(\underline{\underline{I}} - \hat{r}\hat{r}) \cdot \hat{n} \times (\hat{k}_{\text{inc}} \times \hat{p}_{\text{inc}}) - \hat{r} \times (\hat{n} \times \hat{p}_{\text{inc}}) \right]. \quad (\text{C.7})$$

In order to solve the integral, the observation propagation vector \vec{k} can be written in its cartesian components as

$$\vec{k} = \begin{bmatrix} k_x \\ k_y \\ k_z \end{bmatrix} = k_0 \begin{bmatrix} \sin \theta \cos \phi \\ \sin \theta \sin \phi \\ \cos \theta \end{bmatrix}. \quad (\text{C.8})$$

Furthermore, since the domain of integration is a disk, it is convenient to represent the vector \vec{r}' in polar coordinates as follows

$$\vec{r}' = \begin{bmatrix} x' \\ y' \\ 0 \end{bmatrix} = \begin{bmatrix} \rho' \cos \phi' \\ \rho' \sin \phi' \\ 0 \end{bmatrix}. \quad (\text{C.9})$$

The integral in (C.7) can be written as

$$\iint_D e^{jk_{\text{inc},x}x'} e^{jk_{\text{inc},y}y'} e^{jk_x x'} e^{jk_y y'} dx' dy'. \quad (\text{C.10})$$

The integral can be simplified in the following way

$$\begin{aligned} e^{jk_{\text{inc},x}x'} e^{jk_{\text{inc},y}y'} &= e^{-jk\rho' \sin \theta_i (\cos \phi' \cos \phi_i + \sin \phi' \sin \phi_i)} \\ &= e^{-jk\rho' \sin \theta_i \cos(\phi' - \phi_i)} \end{aligned} \quad (\text{C.11})$$

and

$$\begin{aligned} e^{jk_x x'} e^{jk_y y'} &= e^{jk\rho' \sin \theta (\cos \phi' \cos \phi + \sin \phi' \sin \phi)} \\ &= e^{jk\rho' \sin \theta \cos(\phi' - \phi)}. \end{aligned} \quad (\text{C.12})$$

Therefore, considering a disk of radius a , (C.10) becomes

$$\int_0^a \int_0^{2\pi} e^{-jk\rho' \sin \theta_i \cos(\phi' - \phi_i)} e^{jk\rho' \sin \theta \cos(\phi' - \phi)} d\phi' \rho' d\rho'. \quad (\text{C.13})$$

In order to solve the integral in (C.13), first recall that

$$e^{\pm jz \cos \Delta} = \cos(z \cos \Delta) \pm j \sin(z \cos \Delta). \quad (\text{C.14})$$

Recalling [31, Eq. (9.1.44)] and [31, Eq. (9.1.45)], respectively

$$\cos(z \cos \Delta) = J_0(z) + 2 \sum_{k=1}^{\infty} (-1)^k J_{2k}(z) \cos(2k\Delta) \quad (\text{C.15})$$

$$\sin(z \cos \Delta) = 2 \sum_{k=0}^{\infty} (-1)^k J_{2k+1}(z) \cos((2k+1)\Delta) \quad (\text{C.16})$$

allows us to rewrite (C.14) as follows

$$e^{\pm jz \cos \Delta} = J_0(z) + 2 \sum_{k=1}^{\infty} (-1)^k J_{2k}(z) \cos(2k\Delta) \pm 2j \sum_{k=0}^{\infty} (-1)^k J_{2k+1}(z) \cos((2k+1)\Delta). \quad (\text{C.17})$$

Using $2k = n$ in the first sum and $2k+1 = n$ in the second sum leads to

$$e^{\pm jz \cos \Delta} = J_0(z) + 2 \sum_{\substack{n=2 \\ \text{even}}}^{\infty} (-1)^{\frac{n}{2}} J_n(z) \cos(n\Delta) \pm 2j \sum_{\substack{n=1 \\ \text{odd}}}^{\infty} (-1)^{\frac{n-1}{2}} J_n(z) \cos(n\Delta). \quad (\text{C.18})$$

Furthermore, using $j = (-1)^{\frac{1}{2}}$, we can rewrite (C.18) as follows

$$\begin{aligned}
 e^{\pm jz \cos \Delta} &= J_0(z) + 2 \sum_{\substack{n=2 \\ \text{even}}}^{\infty} (-1)^{\frac{n}{2}} J_n(z) \cos(n\Delta) \pm 2(-1)^{\frac{1}{2}} \sum_{\substack{n=1 \\ \text{odd}}}^{\infty} (-1)^{\frac{n-1}{2}} J_n(z) \cos(n\Delta) \\
 &= J_0(z) + 2 \sum_{\substack{n=2 \\ \text{even}}}^{\infty} (-1)^{\frac{n}{2}} J_n(z) \cos(n\Delta) \pm 2 \sum_{\substack{n=1 \\ \text{odd}}}^{\infty} (-1)^{\frac{n}{2}} J_n(z) \cos(n\Delta).
 \end{aligned} \tag{C.19}$$

Two cases are considered. Firstly,

$$\begin{aligned}
 e^{jz \cos \Delta} &= J_0(z) + 2 \sum_{\substack{n=2 \\ \text{even}}}^{\infty} (-1)^{\frac{n}{2}} J_n(z) \cos(n\Delta) + 2 \sum_{\substack{n=1 \\ \text{odd}}}^{\infty} (-1)^{\frac{n}{2}} J_n(z) \cos(n\Delta) \\
 &= J_0(z) + 2 \sum_{n=1}^{\infty} (-1)^{\frac{n}{2}} J_n(z) \cos(n\Delta) = J_0(z) + 2 \sum_{n=1}^{\infty} j^n J_n(z) \cos(n\Delta)
 \end{aligned} \tag{C.20}$$

$$e^{jz \cos \Delta} = J_0(z) + 2 \sum_{n=1}^{\infty} j^n J_n(z) \cos(n\Delta). \tag{C.21}$$

Secondly,

$$\begin{aligned}
 e^{-jz \cos \Delta} &= J_0(z) + 2 \sum_{\substack{n=2 \\ \text{even}}}^{\infty} (-1)^{\frac{n}{2}} J_n(z) \cos(n\Delta) - 2 \sum_{\substack{n=1 \\ \text{odd}}}^{\infty} (-1)^{\frac{n}{2}} J_n(z) \cos(n\Delta) \\
 &= J_0(z) + 2 \sum_{n=1}^{\infty} (-1)^n (-1)^{\frac{n}{2}} J_n(z) \cos(n\Delta) = J_0(z) + 2 \sum_{n=1}^{\infty} (-j)^n J_n(z) \cos(n\Delta)
 \end{aligned} \tag{C.22}$$

$$e^{-jz \cos \Delta} = J_0(z) + 2 \sum_{n=1}^{\infty} (-j)^n J_n(z) \cos(n\Delta). \tag{C.23}$$

Using (C.21) and (C.23) in (C.13) results in

$$\begin{aligned}
 &\int_0^a \int_0^{2\pi} e^{-jk\rho' \sin \theta_i \cos(\phi' - \phi_i)} e^{jk\rho' \sin \theta \cos(\phi' - \phi)} d\phi' \rho' d\rho' = \\
 &\int_0^a \int_0^{2\pi} \left[J_0(k\rho' \sin \theta_i) + 2 \sum_{n=1}^{\infty} (-j)^n J_n(k\rho' \sin \theta_i) \cos(n(\phi_i - \phi')) \right] [J_0(k\rho' \sin \theta) \\
 &\quad + 2 \sum_{m=1}^{\infty} j^m J_m(k\rho' \sin \theta) \cos(m(\phi - \phi'))] d\phi' \rho' d\rho' = \\
 &\int_0^a \int_0^{2\pi} \left[J_0(k\rho' \sin \theta_i) J_0(k\rho' \sin \theta) + 2 J_0(k\rho' \sin \theta_i) \sum_{m=1}^{\infty} j^m J_m(k\rho' \sin \theta) \cos(m(\phi - \phi')) \right. \\
 &\quad \left. + 2 J_0(k\rho' \sin \theta) \sum_{n=1}^{\infty} (-j)^n J_n(k\rho' \sin \theta_i) \cos(n(\phi_i - \phi')) \right. \\
 &\quad \left. + 4 \sum_{n=1}^{\infty} \sum_{m=1}^{\infty} j^m J_m(k\rho' \sin \theta) \cos(m(\phi - \phi')) (-j)^n J_n(k\rho' \sin \theta_i) \cos(n(\phi_i - \phi')) \right] d\phi' \rho' d\rho'.
 \end{aligned} \tag{C.24}$$

Noting that

$$\int_0^{2\pi} \cos(n(\phi_i - \phi')) d\phi' = 0 \quad \forall n \in \mathbb{Z}^+ \quad (\text{C.25})$$

implies that the second and third term in (C.24) vanish, simplifying as follows

$$\begin{aligned} & \int_0^a \int_0^{2\pi} [J_0(k\rho' \sin \theta_i) J_0(k\rho' \sin \theta) \\ & + 4 \sum_{n=1}^{\infty} \sum_{m=1}^{\infty} j^m J_m(k\rho' \sin \theta) \cos(m(\phi - \phi')) (-j)^n J_n(k\rho' \sin \theta_i) \cos(n(\phi_i - \phi'))] d\phi' \rho' d\rho'. \end{aligned} \quad (\text{C.26})$$

Moreover, the integral of a product of two cosines can be written as follows

$$\begin{aligned} & \int_0^{2\pi} \cos(m(\phi - \phi')) \cos(n(\phi_i - \phi')) d\phi' \\ & = \int_0^{2\pi} \frac{1}{2} [\cos(m\phi + n\phi_i - (m+n)\phi') + \cos(m\phi - n\phi_i + (n-m)\phi')] d\phi'. \end{aligned} \quad (\text{C.27})$$

It can be seen that all terms equate to zero, except for the case when $m = n$, for which the integral has the following solution

$$\int_0^{2\pi} \cos(m(\phi - \phi')) \cos(m(\phi_i - \phi')) d\phi' = \pi \cos(m(\phi - \phi_i)). \quad (\text{C.28})$$

Recognizing that $j^n (-j)^n = 1$, we can rewrite (C.26) as follows

$$\begin{aligned} & \int_0^a \left[J_0(k\rho' \sin \theta_i) J_0(k\rho' \sin \theta) 2\pi + 4 \sum_{n=1}^{\infty} J_n(k\rho' \sin \theta) J_n(k\rho' \sin \theta_i) \pi \cos(n(\phi - \phi_i)) \right] \rho' d\rho' = \\ & \int_0^a \left[J_0(k\rho' \sin \theta_i) J_0(k\rho' \sin \theta) 2\pi + 4\pi \sum_{n=1}^{\infty} J_n(k\rho' \sin \theta) J_n(k\rho' \sin \theta_i) \cos(n(\phi - \phi_i)) \right] \rho' d\rho' = \\ & 2\pi \int_0^a J_0(k\rho' \sin \theta_i) J_0(k\rho' \sin \theta) \rho' d\rho' + 4\pi \sum_{n=1}^{\infty} \cos(n(\phi - \phi_i)) \int_0^a J_n(k\rho' \sin \theta) J_n(k\rho' \sin \theta_i) \rho' d\rho'. \end{aligned} \quad (\text{C.29})$$

Recalling the following property [34, Eq. (6.521)]

$$\int_0^1 J_n(\alpha\rho) J_n(\beta\rho) \rho d\rho = \frac{\beta J_{n-1}(\beta) J_n(\alpha) - \alpha J_{n-1}(\alpha) J_n(\beta)}{\alpha^2 - \beta^2} \quad [\alpha \neq \beta, n > -1] \quad (\text{C.30})$$

and using the substitution $\rho' = a\rho$ along with the following property [31, Eq. (9.1.5)]

$$J_{-n}(\rho) = (-1)^n J_n(\rho) \quad (\text{C.31})$$

results in the final expression

$$\begin{aligned} & 2\pi a \frac{\sin \theta_i J_1(ka \sin \theta_i) J_0(ka \sin \theta) - \sin \theta J_0(ka \sin \theta_i) J_1(ka \sin \theta)}{k(\sin^2 \theta_i - \sin^2 \theta)} + 4\pi a \sum_{n=1}^{\infty} \cos(n(\phi - \phi_i)) \\ & \frac{\sin \theta J_n(ka \sin \theta_i) J_{n-1}(ka \sin \theta) - \sin \theta_i J_{n-1}(ka \sin \theta_i) J_n(ka \sin \theta)}{k(\sin^2 \theta_i - \sin^2 \theta)}. \end{aligned} \quad (\text{C.32})$$

D. Radiation from a Tapered Distribution

This appendix presents the derivation of the electric and magnetic far field radiated by a Gaussian tapered current distribution with linear phase on a rectangular aperture.

First, we recall uniform currents on the aperture which can be described as follows

$$\vec{J} = \frac{1}{\zeta} |E_0| e^{j\vec{k}_{\text{scan}}\vec{r}'} \hat{n} \times (\hat{k}_{\text{scan}} \times \hat{p}_{\text{scan}}) \quad (\text{D.1a})$$

$$\vec{M} = |E_0| e^{j\vec{k}_{\text{scan}}\vec{r}'} \hat{n} \times \hat{p}_{\text{scan}}. \quad (\text{D.1b})$$

Recalling the radiation integral in (2.39) for the electric far field and substituting (D.1a) and (D.1b), while applying a Gaussian taper, we can write (2.39) as follows

$$\begin{aligned} \vec{E}(\vec{r}) = & -j\omega\mu \frac{e^{-jkr}}{4\pi r} (\underline{\underline{I}} - \hat{r}\hat{r}) \cdot \iint_S \frac{1}{\zeta} |E_0| e^{j\vec{k}_{\text{scan}}\vec{r}'} \hat{n} \times (\hat{k}_{\text{scan}} \times \hat{p}_{\text{scan}}) e^{j\vec{k}\vec{r}'} d\vec{r}' \\ & + jk \frac{e^{-jkr}}{4\pi r} \hat{r} \times \iint_S |E_0| e^{j\vec{k}_{\text{scan}}\vec{r}'} (\hat{n} \times \hat{p}_{\text{scan}}) e^{j\vec{k}\vec{r}'} d\vec{r}'. \end{aligned} \quad (\text{D.2})$$

By rearranging the terms in (D.2) it can be rewritten as

$$\begin{aligned} \vec{E}(\vec{r}) = & -j\omega\mu \frac{1}{\zeta} |E_0| \frac{e^{-jkr}}{4\pi r} (\underline{\underline{I}} - \hat{r}\hat{r}) \cdot \hat{n} \times (\hat{k}_{\text{scan}} \times \hat{p}_{\text{scan}}) \iint_S e^{j\vec{k}_{\text{scan}}\vec{r}'} e^{j\vec{k}\vec{r}'} d\vec{r}' \\ & + jk |E_0| \frac{e^{-jkr}}{4\pi r} \hat{r} \times (\hat{n} \times \hat{p}_{\text{scan}}) \iint_S e^{j\vec{k}_{\text{scan}}\vec{r}'} e^{j\vec{k}\vec{r}'} d\vec{r}'. \end{aligned} \quad (\text{D.3})$$

Recognizing that $\omega\mu \frac{1}{\zeta} = k$ we can rewrite (D.3) as follows

$$\vec{E}(\vec{r}) = -jk |E_0| \frac{e^{-jkr}}{4\pi r} \iint_S e^{j\vec{k}_{\text{scan}}\vec{r}'} e^{j\vec{k}\vec{r}'} d\vec{r}' \left[(\underline{\underline{I}} - \hat{r}\hat{r}) \cdot \hat{n} \times (\hat{k}_{\text{scan}} \times \hat{p}_{\text{scan}}) - \hat{r} \times (\hat{n} \times \hat{p}_{\text{scan}}) \right]. \quad (\text{D.4})$$

In order to solve the integral, the observation propagation vector \vec{k} can be written in its cartesian components as

$$\vec{k} = \begin{bmatrix} k_x \\ k_y \\ k_z \end{bmatrix} = k_0 \begin{bmatrix} \sin \theta \cos \phi \\ \sin \theta \sin \phi \\ \cos \theta \end{bmatrix}. \quad (\text{D.5})$$

Furthermore, the domain of integration can be represented by the vector \vec{r}' as follows

$$\vec{r}' = \begin{bmatrix} x' \\ y' \\ 0 \end{bmatrix}. \quad (\text{D.6})$$

Moreover, considering that the antenna structure has size S_x along the x direction and S_y along the y direction, the integral in (D.4) can be rewritten as follows

$$\begin{aligned} \iint_S e^{-\left(\frac{x'}{w_x}\right)^2} e^{-\left(\frac{y'}{w_y}\right)^2} e^{j\vec{k}_{\text{scan}}\vec{r}'} e^{j\vec{k}\vec{r}'} d\vec{r}' = & \int_{-S_x/2}^{S_x/2} e^{-\left(\frac{x'}{w_x}\right)^2} e^{j(k_{\text{scan},x} + k_x)x'} dx' \\ & \int_{-S_y/2}^{S_y/2} e^{-\left(\frac{y'}{w_y}\right)^2} e^{j(k_{\text{scan},y} + k_y)y'} dy'. \end{aligned} \quad (\text{D.7})$$

For the sake of simplicity we will only look at one of the integrals, the one along the x direction, the results are applicable for the integral in y . In order to solve the integral we can separate it in two parts as follows

$$\int_{-S_x/2}^{S_x/2} e^{-\left(\frac{x'}{w_x}\right)^2} e^{j(k_{\text{scan},x}+k_x)x'} dx' = \int_{-S_x/2}^0 e^{-\left(\frac{x'}{w_x}\right)^2} e^{j(k_{\text{scan},x}+k_x)x'} dx' + \int_0^{S_x/2} e^{-\left(\frac{x'}{w_x}\right)^2} e^{j(k_{\text{scan},x}+k_x)x'} dx'. \quad (\text{D.8})$$

If we introduce the coordinate transformation $x' = -x$ in the first integral can be written as follows

$$\int_{S_x/2}^0 e^{-\left(\frac{-x}{w_x}\right)^2} e^{-j(k_{\text{scan},x}+k_x)x}(-dx) + \int_0^{S_x/2} e^{-\left(\frac{x'}{w_x}\right)^2} e^{j(k_{\text{scan},x}+k_x)x'} dx' = \int_0^{S_x/2} e^{-\left(\frac{x}{w_x}\right)^2} e^{-j(k_{\text{scan},x}+k_x)x} dx + \int_0^{S_x/2} e^{-\left(\frac{x'}{w_x}\right)^2} e^{j(k_{\text{scan},x}+k_x)x'} dx'. \quad (\text{D.9})$$

These two integrals can be combined as follows

$$\int_0^{S_x/2} e^{-\left(\frac{x}{w_x}\right)^2} \left(e^{j(k_{\text{scan},x}+k_x)x'} + e^{-j(k_{\text{scan},x}+k_x)x} \right) dx' = \int_0^{S_x/2} e^{-\left(\frac{x'}{w_x}\right)^2} 2 \cos((k_{\text{scan},x} + k_x) x') dx'. \quad (\text{D.10})$$

This integral is known and its solution involves the error function as follows

$$\int_{-S_x/2}^{S_x/2} e^{-\left(\frac{x'}{w_x}\right)^2} e^{j(k_{\text{scan},x}+k_x)x'} dx' = \frac{w_x}{2} \sqrt{\pi} e^{-\frac{w_x^2(k_{\text{scan},x}+k_x)^2}{4}} \left[\text{erf}\left(\frac{j(k_{\text{scan},x}+k_x)w_x^2 + S_x}{2w_x}\right) - \text{erf}\left(\frac{j(k_{\text{scan},x}+k_x)w_x^2 - S_x}{2w_x}\right) \right]. \quad (\text{D.11})$$

The derivation in the case of y is similar.

Acronyms

BER bit error rate. 33

C.I. confidence interval. 33

FoV Field of View. 32–34

GUI Graphical User Interface. 46

LoS Line-of-Sight. 2

MIMO Multiple-input multiple-output. III, 1

PO Physical Optics. 2, 9, 10, 12–15, 17, 18, 21, 45, 47, 49, 51, 53

PWS Plane Wave Spectrum. 47

SIR Signal to Interference Ratio. III, 1–3, 25, 26, 29–35, 37–40, 45, 46

SNR Signal to Noise Ratio. 33

This Page Intentionally Left Blank

Bibliography

- [1] J. G. Andrews, T. Bai, M. N. Kulkarni, A. Alkhateeb, A. K. Gupta, and R. W. Heath, "Modeling and Analyzing Millimeter Wave Cellular Systems," *IEEE Transactions on Communications*, vol. 65, no. 1, pp. 403–430, 1 2017.
- [2] T. Schneider, A. Wiatrek, S. Preussler, M. Grigat, and R. P. Braun, "Link budget analysis for terahertz fixed wireless links," *IEEE Transactions on Terahertz Science and Technology*, vol. 2, no. 2, pp. 250–256, 3 2012.
- [3] M. Arias Campo, D. Blanco, S. Bruni, A. Neto, and N. Llombart, "On the Use of Fly's Eye Lenses with Leaky-Wave Feeds for Wideband Communications," *IEEE Transactions on Antennas and Propagation*, vol. 68, no. 4, pp. 2480–2493, 4 2020.
- [4] K. S. Rao, M. Q. Tang, G. A. Morin, and K. K. Chan, "Development of a 45 GHz Multiple-Beam Antenna for Military Satellite Communications," *IEEE Transactions on Antennas and Propagation*, vol. 43, no. 10, pp. 1036–1047, 1995.
- [5] S. K. Rao, "Design and analysis of multiple-beam reflector antennas," *IEEE Antennas and Propagation Magazine*, vol. 41, no. 4, pp. 53–69, 8 1999.
- [6] S. K. Rao, C. C. Hsu, and K. K. Chan, "Antenna system supporting multiple frequency bands and multiple beams," *IEEE Transactions on Antennas and Propagation*, vol. 56, no. 10, pp. 3327–3329, 2008.
- [7] N. Llombart, A. Neto, G. Gerini, M. Bonnedal, and P. De Maagt, "Leaky wave enhanced feed arrays for the improvement of the edge of coverage gain in multibeam reflector antennas," *IEEE Transactions on Antennas and Propagation*, vol. 56, no. 5, pp. 1280–1291, 5 2008.
- [8] T. N. Kaifas, D. G. Babas, G. Toso, and J. N. Sahalos, "Multibeam antennas for global satellite coverage: theory and design," *IET Microwaves, Antennas & Propagation*, vol. 10, no. 14, pp. 1475–1484, 11 2016.
- [9] O. M. Bucci and G. Franceschetti, "On the Degrees of Freedom of Scattered Fields," *IEEE Transactions on Antennas and Propagation*, vol. 37, no. 7, pp. 918–926, 1989.
- [10] P. S. Kildal, E. Martini, and S. MacI, "Degrees of Freedom and Maximum Directivity of Antennas: A bound on maximum directivity of nonsuperreactive antennas," *IEEE Antennas and Propagation Magazine*, vol. 59, no. 4, pp. 16–25, 8 2017.
- [11] C. Ehrenborg and M. Gustafsson, "Physical Bounds and Radiation Modes for MIMO Antennas," *IEEE Transactions on Antennas and Propagation*, vol. 68, no. 6, pp. 4302–4311, 6 2020.
- [12] C. Ehrenborg, M. Gustafsson, and M. Capek, "Capacity Bounds and Degrees of Freedom for MIMO Antennas Constrained by Q-Factor," *IEEE Transactions on Antennas and Propagation*, vol. 69, no. 9, pp. 5388–5400, 9 2021.
- [13] A. Tornese, A. Clemente, and C. Delaveaud, "A New Method for Gain Prediction of Superdirective End-Fire Arrays," *2022 16th European Conference on Antennas and Propagation, EuCAP 2022*, 2022.
- [14] V. Shyianov, M. Akrouf, F. Bellili, A. Mezghani, and R. W. Heath, "Achievable Rate with Antenna Size Constraint: Shannon Meets Chu and Bode," *IEEE Transactions on Communications*, vol. 70, no. 3, pp. 2010–2024, 3 2022.
- [15] S. Stein, "On Cross Coupling in Multiple-Beam Antennas," *IRE Transactions on Antennas and Propagation*, vol. 10, no. 5, pp. 548–557, 1962.

- [16] A. Neto, N. Llombart, and A. Freni, "The Observable Field for Antennas in Reception," *IEEE Transactions on Antennas and Propagation*, vol. 66, no. 4, pp. 1736–1746, 4 2018.
- [17] R. Ozzola, D. Cavallo, A. Freni, N. Llombart, and A. Neto, "A Benchmark for the Number of Independent Line of Sight Links on a Given Volume Platform," *IEEE Transactions on Antennas and Propagation*, pp. 1–1, 9 2022.
- [18] A. Neto, A. F. Bernardis, D. Emer, A. Freni, and N. Llombart, "The Observable Field in Complex Scattering Scenarios," *IEEE Transactions on Antennas and Propagation*, vol. 68, no. 7, pp. 5544–5555, 7 2020.
- [19] J. B. Andersen and A. Frandsen, "Absorption efficiency of receiving antennas," *IEEE Transactions on Antennas and Propagation*, vol. 53, no. 9, pp. 2843–2849, 9 2005.
- [20] M. Gustafsson, M. Cismasu, and B. L. Jonsson, "Physical bounds and optimal currents on antennas," *IEEE Transactions on Antennas and Propagation*, vol. 60, no. 6, pp. 2672–2681, 2012.
- [21] D. H. Kwon and D. M. Pozar, "Optimal characteristics of an arbitrary receive antenna," *IEEE Transactions on Antennas and Propagation*, vol. 57, no. 12, pp. 3720–3727, 12 2009.
- [22] J. A. Stratton, *Electromagnetic Theory*. John Wiley & Sons, Inc., 10 2015.
- [23] R. F. Harrington, *Time-harmonic electromagnetic fields*. IEEE Press, 2001.
- [24] P. S. Kildal and S. R. Best, "Further investigations of fundamental directivity limitations of small antennas with and without ground planes," *2008 IEEE International Symposium on Antennas and Propagation and USNC/URSI National Radio Science Meeting, APSURSI*, 2008.
- [25] A. Pascual Laguna, D. Cavallo, J. J. Baselmans, and N. Llombart, "Focused Connected Array Antenna as a Broadband Beam-Steering Feed for Quasi-Optical System," *IEEE Transactions on Antennas and Propagation*, vol. 70, no. 7, pp. 5995–6000, 7 2022.
- [26] V. H. Rumsey, "On the Design and Performance of Feeds for Correcting Spherical Aberration," *IEEE Transactions on Antennas and Propagation*, vol. AP-18, no. 3, pp. 343–351, 1970.
- [27] K. Atkinson and W. Han, *Spherical Harmonics and Approximations on the Unit Sphere: An Introduction*, ser. Lecture Notes in Mathematics. Berlin, Heidelberg: Springer Berlin Heidelberg, 2012, vol. 2044. [Online]. Available: <http://link.springer.com/10.1007/978-3-642-25983-8>
- [28] E. Darve, "The Fast Multipole Method: Numerical Implementation," *Journal of Computational Physics*, vol. 160, pp. 195–240, 2000.
- [29] C. H. L. Beentjes, "Quadrature on a Spherical Surface," Mathematical Institute, University of Oxford, Tech. Rep., 2015. [Online]. Available: <https://cbeentjes.github.io/files/Ramblings/QuadratureSphere.pdf>
- [30] A. Mazzinghi and A. Freni, "Analytical Evaluation of the Power Radiated by Sources Arbitrarily Distributed on a Surface," *IEEE Transactions on Antennas and Propagation*, 2022.
- [31] M. Abramowitz and I. A. Stegun, *Handbook of mathematical functions: with formulas, graphs, and mathematical tables*. Dover Publications, 1972.
- [32] L. W. Couch, *Digital and analog communication systems*, 8th ed. Pearson, 2013.

- [33] P. F. Goldsmith, "Radiation patterns of circular apertures with Gaussian illumination," *International Journal of Infrared and Millimeter Waves* 1987 8:7, vol. 8, no. 7, pp. 771–781, 1987.
- [34] A. Jeffrey and D. Zwillinger, *Table of integrals, series, and products: Seventh edition*. Academic Press, 2 2007.